arXiv:1606.02372v1 [q-bio.NC] 8 Jun 2016

Entrainment of traveling waves to rhythmic motor acts

Joaquín Rapela*
Swartz Center for Computation Neuroscience
University of California San Diego

June 9, 2016

Abstract

A remarkable early observation on brain dynamics is that when humans are exposed to rhythmic stimulation their brain oscillations entrain to the rhythm of the stimuli (Adrian and Matthews, 1934). Currently it is not know whether rhythmic motor acts can entrain neural oscillations. We investigated this possibility in an experiment where a subject produced consonant-vowel (CV) syllables in a rhythmic fashion, while we performed ECoG recordings with a dense grid covering most speech processing brain regions across the left hemisphere. Most strongly over the ventral sensorimotor cortex (vSMC), a cortical region that controls the vocal articulators, we detected significant concentration of phase across trials at the specific frequency of speech production. We also observed amplitude modulations. In addition we found significant coupling between the phase of brain oscillations at the frequency of speech production and their amplitude in the high-gamma range (i.e., phase-amplitude coupling, PAC). Furthermore, we saw that brain oscillations at the frequency of speech production organized as traveling waves (TWs), synchronized to the rhythm of speech production. It has been hypothesized that PAC is a mechanism to allow low-frequency oscillations to synchronize with high-frequency neural activity so that spiking occurs at behaviorally relevant times. If this hypothesis is true, when PAC coexists with TWs, we expect a specific organization of PAC curves. We observed this organization experimentally and verified that the peaks of high-gamma oscillations, and therefore spiking, occur at the same times across electrodes. Importantly, we observed that these spiking times were synchronized with the rhythm of speech production. To our knowledge, this is the first report of motor actions organizing (a) the phase coherence of low-frequency brain oscillations, (b) the coupling between the phase of these oscillations and the amplitude of high-frequency oscillations, and (c) TWs. It is also the first demonstration that TWs induce an organization of PAC so that spiking across spatial locations is synchronized to behaviorally relevant times.

*rapela@ucsd.edu

Glossary

CV consonant vowel.

ECoG electrocorticography. A brain recording modality that measures potentials directly from the cortical surface.

EEG electroencephalography. A brain recording modality that measures electrical potentials from the scalp..

ERP event-related potential. Mean of voltages recorded at a single electrode and aligned with respect to an event of interest (e.g., the transition time between a consonant and a vowel)..

ERSP event-related spectral perturbation. An average measure of evoked power across trials (Section A.1.3).

ITC inter-trial coherence. A measure of phase alignment between trials (Section A.1.2).

MEG magnetoencephalography. A brain recording modality that measures magnetic fields from the scalp..

MI modulation index quantifying the strength of phase-amplitude coupling (Sections 2.3 and A.1.4).

PAC phase-amplitude coupling. Coupling between the phase of low-frequency oscillations and the amplitude of high-frequency ones (Sections 2.3 and A.1.4).

TW traveling wave (Section 2.4).

vSMC ventral sensorimotor cortex. A brain region that controls the vocal articulators.

Contents

1 Introduction **1**

2 Results **2**
2.1 Phase Alignment 2
2.2 Amplitude Modulations 4
2.3 Phase-Amplitude Coupling (PAC) 5
2.4 Traveling Waves (TWs) 7
2.5 Organization of PAC in the Presence of TWs 9

3 Discussion **10**

4 Acknowledgments **13**

A Supplementary Information **2**
A.1 Methods 2
A.1.1 Circular statistics concepts 2
A.1.2 ITC 2
A.1.3 ERSP 2
A.1.4 Phase-amplitude coupling curve and modulation index . . 3
A.2 Behavioral Data 3
A.3 ITC across the vSMC 3
A.4 ERSPs across the vSMC 16
A.5 ERPs across the vSMC 34
A.6 Electrodes with strongest PAC 34

1 Introduction

External visual (Regan, 1966) and auditory (Galambos et al., 1981) rhythmic stimuli entrain brain oscillations (i.e., drag brain oscillations to follow the rhythm of the stimuli), and this entrainment is modulated by attention so that the occurrence of attended stimuli coincides with the phase of brain oscillations of maximal excitability (Lakatos et al., 2005, 2008, 2013; O'Connell et al., 2011; Besle et al., 2011; Gomez-Ramirez et al., 2011; Zion Golumbic et al., 2013; Cravo et al., 2013; Mathewson et al., 2010; Spaak et al., 2014; Gray et al., 2015). Although speech is only quasi rhythmic (Cummins, 2012) an increasing number of studies is showing that neural oscillations can entrain to speech sound (e.g., Zion Golumbic et al., 2013; Gross et al., 2013; Doelling et al., 2014; Millman et al., 2015; Park et al., 2015). For recent reviews on the entrainment of neural oscillations to speech sound see Peelle and Davis (2012); Zion Golumbic et al. (2012); Ding and Simon (2014). What is currently not know if whether speech production can entrain neural oscillations. Here we present evidence showing that a speaker rhythmically producing consonant-vowel (CV) syllables at different frequencies entrains brain oscillations in the ventral sensorimotor cortex (vSMC) at corresponding different frequencies.

It has been suggested that a role of entrained low-frequency oscillations is to modulate the excitability of neurons, in such a way that periods of higher excitability correspond to events of interest in sensory streams (Schroeder and Lakatos, 2009). This hypothesis has been supported by reports of phase-amplitude coupling (PAC), where the phase of low-frequency oscillations modulates the amplitude of higher-frequency ones (e.g., Canolty et al., 2006). In speech perception it has been proposed that theta rhythm (3-8 Hz) is related to the encoding of slower syllabic information in the speech signal, the gamma rhythm (>30 Hz) is involved in the linguistic coding of phonemic details, and the PAC between the theta and gamma rhythms could modulate the excitability of neurons to devote more processing power to the informative parts of syllabic sound patterns (Giraud and Poeppel, 2012; Hyafil et al., 2015). However, PAC has not yet been reported in speech-production brain regions. We show that over the vSMC the low-frequency oscillations entrained to the rhythm of speech production are strongly coupled with high-gamma oscillations. Importantly, we demonstrate that the phase at which the entrained oscillation couples with the maximum amplitude of the high-gamma oscillations changes orderly from ventral to dorsal electrodes over the vSMC.

Traveling waves (TWs) have been reported in animal studies (e.g., Rubino et al., 2006), human EEG (e.g., Patten et al., 2012), and human ECoG (e.g., Bahramisharif et al., 2013). However, these waves have not been observed in speech production brain regions in humans. The aforementioned orderly change of PAC across the vSMC suggested the existence of TWs. We looked for them and we found them. As mentioned above, brain activity at single recording sites can be entrained to external stimulation but, to our knowledge, it is unknown whether distributed spatio-temporal activity in the form of TWs can also be entrained. We demonstrate that TWs over the vSMC are entrained to the rhythm of speech produc-

tion.

PAC has been studied in the absence of TWs. When these waves are present, in order for cells to fire at the same behaviorally-relevant time, PAC curves measured across electrodes should be different from each other and systematically organized. If these curves were identical to each other, cells would fire in the order given by the propagating TW, and not at the same time. Below we propose an organization of PAC so that when TWs are present cells fire at the same time, we show that this organization is present in our recordings, and provide evidence indicating that cells along the direction of propagation of a planar TW fire at the same behaviorally relevant time.

2 Results

2.1 Phase Alignment

We epoched the raw ECoG waveforms around the time of CV transitions (represented by the vertical line at time zero in all figures). We analyzed separately recordings from different sessions, and present the analysis from recording sessions EC2_B105 and EC2_B89, the sessions with the largest (1.62 sec) and shortest (0.97 sec) median inter-syllable separation times, respectively (Figure A.1). Figure 1a and 1b show the inter-trial coherence (ITC, Section A.1.2), a measure of phase alignment in a group of trials, calculated from recordings in sessions EC2_B105 and EC2_B89, respectively, for electrode 154 in the vSMC (Figure 2). In agreement with our hypothesis that the rhythm of speech production entrains low-frequency brain oscillations, in the ITC computed from data from experimental session EC2_B105 with a median inter-syllable production frequency of 0.62 Hz (black horizontal line in Figure 1a), we observe a peak of ITC around this frequency (red pixels in Figure 1a). Also, we see a peak of ITC around a frequency of 1.03 Hz in Figure 1b, obtained from an experimental session where the median inter-syllable separation time was 1.03 Hz. These figures illustrate that low-frequency brain oscillations entrain to the rhythm of speech production.

For each electrode, we computed the maximum ITC between 0.5 seconds before and 0.6 seconds after the CV transition at the frequency of speech production. Figure 2 highlights the 50 electrodes with largest ITCs. We sorted the electrodes by their maximum ITC value, and colored them according to their rank in this sorting. The ten electrodes with largest ITC are colored in red and are located in the center of the ventral sensoritmotor cortex. As the distance of an electrode to the center of the vSMC increases, its maximum ITC decreases. Section A.3 more clearly illustrates the specificity of phase coherence to the vSMC by showing ITC plots from the ventral to the dorsal edge of the grid across the vSMC.

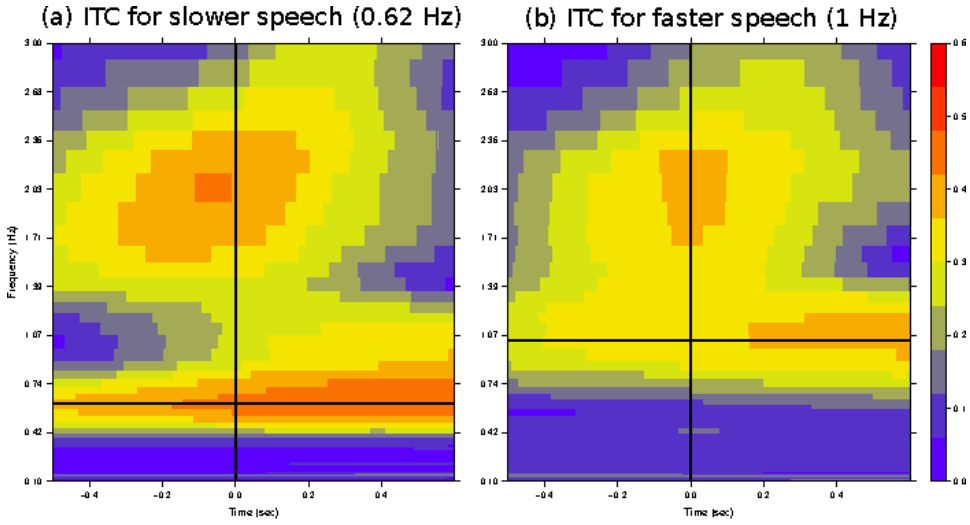

Figure 1: ITCs for electrode 154 computed from recordings in experimental session EC2_B105 with an inter-syllable production frequency of 0.62 Hz (a), and from experimental session EC2_B89 with an inter-syllable production frequency of 1.03 Hz (b). Note that the peaks of the ITC at the lowest frequencies (red points) align with the median frequency of speech production (black horizontal line) both when the subject speaks slower (a) and faster (b).

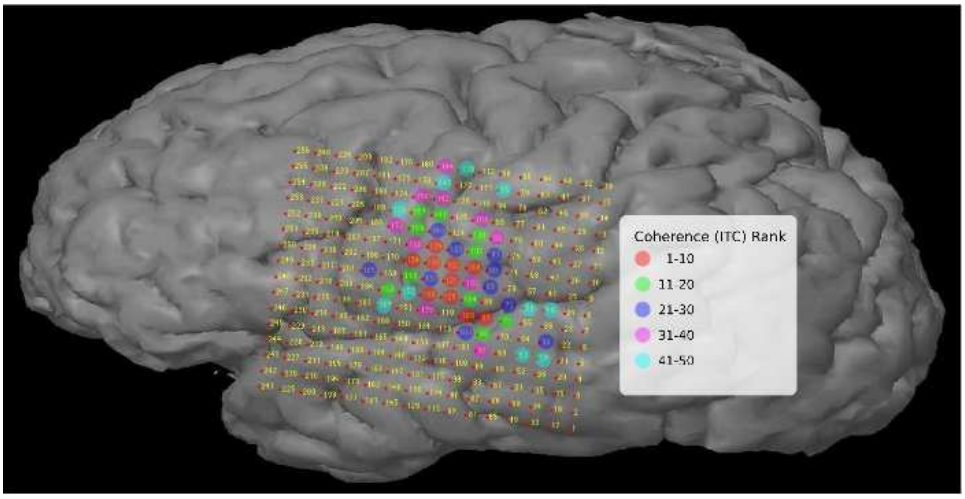

Figure 2: Strongest entrainment occurs over the vSMC. The 50 electrodes with largest ITC (between 0.5 seconds before and 0.6 seconds after the CV transition, at the frequency of CV production, in the experimental session EC2_B105) are highlighted in color.

2.2 Amplitude Modulations

The Event-Related Spectral Perturbation (ERSP, Section A.1.3) is a measure of power modulations around an event of interest. Figure 3a shows ERSPs around the transition time between consonants and vowels (black vertical line in Figure 3). In electrode 133 over auditory cortex (Figure 3a) we see a significant power increase (red blob) before the transition between consonants and vowels in the beta range. Differently, in electrode 135 over the vSMC (Figure 3b) we observe a significant power increase after the transition between consonants and vowels and in the high-gamma range.

Figures A.18-A.30 show ERSPs between the ventral electrode 129 and the dorsal electrode 141 in experimental session EC2_B105. Power in the beta range increases from electrodes 129 to 132 (Figures A.18-A.21) in the ventral temporal cortex, and peaks over electrodes 133 and 134 around the auditory cortex (Figures A.22 and A.23), prior to consonant-vowel transitions. A sharp transition is seen in electrode 135 over the ventral sensorimotor cortex (Figure A.24), with strong modulations in the high-gamma range (70-200 Hz), after consonant-vowel transitions, and almost no modulation in the beta range. This pattern of modulations is strongest over electrode 136 (Figure A.25), and fades along electrodes 137-141 (Figures A.26-A.30) toward the dorsal end of the vSMC.

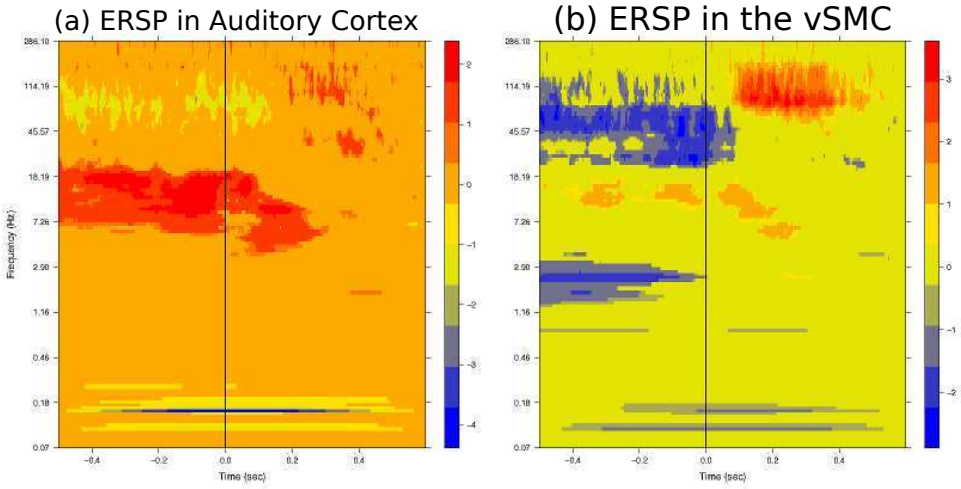

Figure 3: ERSPs for electrode 133 in the auditory cortex (a) and for electrode 135 in the vSMC (b). In the auditory cortex (a) we observe a peak of amplitude (red blob) in the beta range before the CV transition (vertical black line), while in the vSMC (b) a peak of amplitude occurs in the high-gamma range after the CV transition.

2.3 Phase-Amplitude Coupling (PAC)

For experimental session EC2_B105, we studied the coupling between phase at the entrainment frequency of 0.62 Hz (0.01 Hz, wavelet full width at half maximum) and amplitude at 100 Hz (2.06 Hz, wavelet full width at half maximum). For each electrode we calculated the PAC curve (Section A.1.4), and quantified the strength of the coupling using the modulation index (MI, Section A.1.4). Figure 4 shows PAC curves measured at electrodes 135-138 (for visualization purposes we show two phase cycles). The ECoG power at 100 Hz is well modulated by the phase at the entrainment frequency, with MIs 4.84e-3, 8.22e-3, 1.05e-3, and 2.82e-3 at electrodes 135-138, respectively. For electrode 136 (green trace) larger ECoG amplitudes in the high-gamma range (100 Hz) tend to occur at the valley (phase near π) of the low-frequency oscillation (0.62 Hz). As we move from the more ventral electrode 135 to the more dorsal electrode 138, the phase of the low-frequency oscillation at which the amplitude of the high-gamma oscillations is maximal shifts gradually from π (pink trace) to 0 (violet trace). We discuss this organization in Section 2.5. Strongest PAC between phase at the entrainment frequency and amplitude at 100 Hz was observed over the vSMC and surrounding regions. Figure A.44 highlights the 50 electrodes with largest MI.

For electrode 154 in the vSMC, we computed the MI for all pairs of frequency for phase and frequency for amplitude, with the frequency for phase between

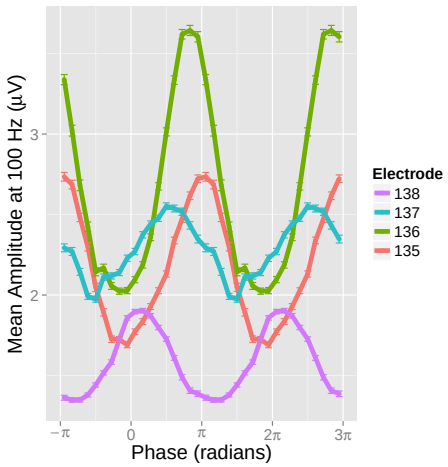

Figure 4: Phase-amplitude coupling curves at electrodes over the vSMC. Phase and amplitude were measured at the entrainment frequency (0.62 Hz) and at 100 Hz, respectively. All displayed electrodes showed a strong modulation of the high-gamma amplitude by the entrained low-frequency phase. Note that as we move from more ventral to more dorsal electrodes (i.e., from electrode 135 to electrode 138) the peak of the PAC curves occurs at earlier phases. The significance of this organization is discussed in Section 2.5.

0.1 and 20 Hz, and the frequency for amplitude between 5 and 200 Hz. We only observed large MIs for frequencies for phase between 0.1 and 2 Hz. Figure 5a plots the obtained MIs. We found two clusters of the frequency for amplitude with large MIs. The first cluster was on the high-gamma range (60 to 150 Hz) and the second cluster on the beta range (20 to 40 Hz). An asterisk in Figure 5 marks a MI peak, the number next to the asterisk is the peak MI, and the first and second numbers in the parenthesis are the frequency for phase and for amplitude, respectively, of the peak MI. Interestingly, for the cluster on the high-gamma range, the maximum MI occurred exactly at the bin of the entrainment frequency (0.62 Hz for the frequency for phase). Differently, for the cluster in beta range the maximum MI occurred below the entrainment frequency (0.5 Hz for the frequency for phase). This figure suggests that not only low-frequency oscillations become entrained to the rhythm of speech production, but also PAC is optimized at this rhythm. For electrode 132 in the auditory cortex, Figure 5b, the MIs were overall much weaker, and both the clusters in the high-gamma and beta ranges showed a peak MI at frequencies for phase below the entrainment frequency. This suggest that the maximization of PAC at the entrainment frequency is specific to the vSMC.

2.4 Traveling Waves (TWs)

We filtered the ECoG recordings in experimental session EC2_B105 (Figure A.1) with a second-order bandpass Butterworth filter around the median syllable-production syllable of 0.62 Hz (low- and high-frequency cutoffs 0.4 Hz and 0.8 Hz, respectively). Figure 6 shows the filtered voltages from electrodes 135-141 at the center of the vSMC in a representative time interval (390 to 400 seconds after the start of the experiment). We see that, as we move from the ventral electrode 135 to the dorsal electrode 141, the voltage traces are orderly shifted to later times. The vertical black lines indicate the transition time between a consonant and a vowel in the production of consonant-vowel syllables. Note that the peaks of the voltage traces tend to occur around these consonant-vowel transition times. Thus, this figure illustrates a wave of activity traveling from the ventral to the dorsal edge of the ventral sensorimotor cortex and entrained to the rhythm of speech production.

A movie showing the cosine of the phase of the bandpassed filtered voltages across the whole grid simultaneously with the speech of the subject can be found at `https://youtu.be/dXrzj2eEuVY`. The bottom/top/left/right pixels in the movie correspond to electrodes along the ventral/dorsal/frontal/caudal sides of the grid. We see mostly planar traveling waves moving in different directions, but occasionally we also observe rotating traveling waves. At most times when the subject produces a CV syllable we see a white blob over the vSMC, indicating that filtered voltages approach their peak values. This movie demonstrates, for the first time, the existence of traveling waves across left speech processing brain areas synchronized to the rhythm of speech production.

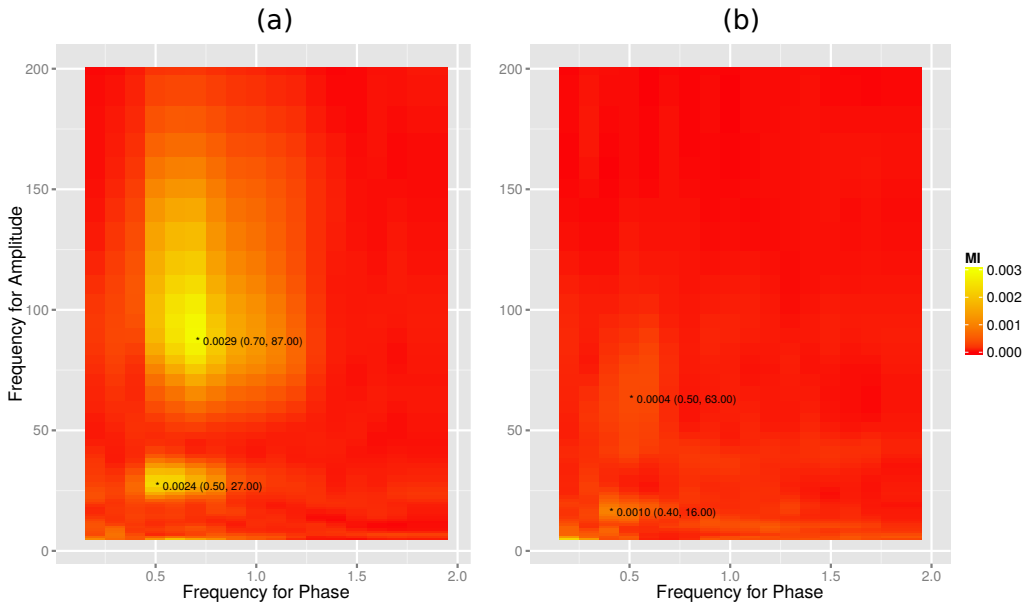

Figure 5: Modulation indices for electrode 154 over the vSMC (a) and for electrode 132 over the auditory cortex (b) at multiple frequencies for phase and amplitude. Over the vSMC (a) the peak MI for amplitudes in the high-gamma range occurs at the entrained frequency for phase (0.62 Hz), while the peak MI for amplitudes in the beta range occurs at lower frequencies. This suggests that over the vSMC not only phase coherence, but also phase-amplitude coupling, is matched to the speech production frequency. Over auditory cortex (b) MIs are much smaller than over the vSMC and the peak MIs occurred at frequencies for phase below the entrainment frequency. This suggests that PAC is largest over speech-production brain regions and that the maximization of PAC at the entrainment frequency is specific to the vSMC.

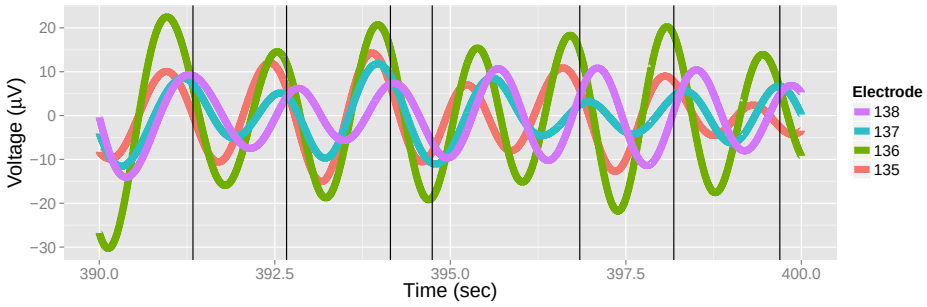

Figure 6: Filtered voltage waveforms along the ventral-dorsal axis of the vSMC. Filtering was performed between 0.4 and 0.8 Hz, around the median frequency of CV syllable production of 0.62 Hz. Vertical black lines indicate CV transition times. As we move from the ventral electrode 135 in red to the dorsal electrode 141 in magenta, voltage waveforms are orderly shifted to right, indicating the existence of a traveling wave. Also, the peak of the waves occurs around the time of CV transitions, suggesting that these traveling waves are entrained to the rhythm of speech production.

2.5 Organization of PAC in the Presence of TWs

If we wanted to design a brain so that all neurons recorded by the four electrodes in Figure 4 fired at the same behaviorally relevant time (e.g., the transition between the consonant-vowel syllable at time 391.2 seconds), how would be choose the PAC curves for these electrodes? Since the phase at electrode 135 (red trace in Figure 4) at time 391.2 is close to $\pi/4$ we would use a PAC curve for this electrode with maximal high-gamma amplitude at this phase. Then, because high-gamma amplitude is related to neural firing (Ray et al., 2008), cells around electrode 135 would then tend to spike at the time of the consonant vowel transition. Next, due to the traveling wave, the phase at electrode 136 at time 391.2 is earlier than that at electrode 135, thus we would use a PAC curve with a peak at this earlier phase for electrode 136. Similarly, we would use a PAC curve with an earlier peak at electrode 137 than that at electrode 136. That is, as we move along the direction of propagation of a traveling wave, we would use PAC curves with earlier and earlier peaks. And this is what we observed experimentally in Figure 4.

To validate that the previous organization of PAC curves allows cells to fire at the same behaviorally relevant time in the presence of traveling waves, Figure 7 plots mean high-gamma amplitude as a function of time for electrodes 135-138 (for each time and each electrode, we extracted the phase at 0.62 Hz, then the mean amplitude at 100 Hz for this phase from the PAC curve in Figure 4, and finally we plotted the extracted mean amplitudes as a function of the corresponding times). As expected, we found that high-gamma amplitude, and

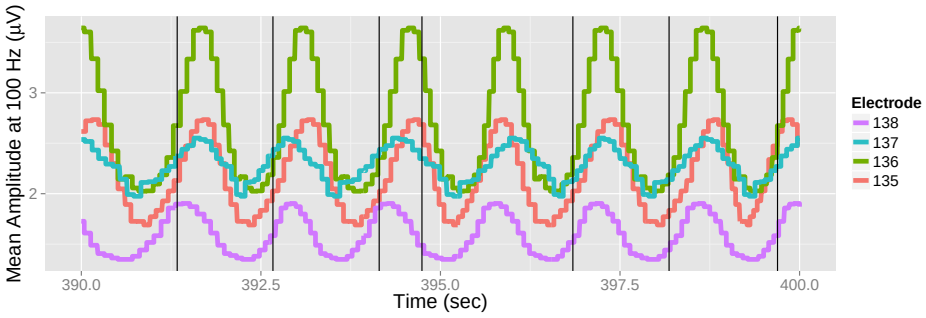

Figure 7: Mean high-gamma amplitude as a function of time at electrodes over the ventral sensorimotor cortex. Each time point at each electrode corresponds to a given phase of the oscillation at the speech-production frequency of 0.62 Hz in Figure 6, and from Figure 4 each phase corresponds to a given mean amplitude at 100 Hz. Thus, each time point of each electrode corresponds to a mean phase at 100 Hz. Colored traces show this correspondence across different electrodes. We observe that mean high-gamma amplitude, and therefore spiking, is aligned across electrodes over the ventral sensorimotor cortex and synchronized to the rhythm of speech production. The curves are not smooth because we used coarse bins in the calculation of the PAC curves in Figure 4.

therefore cell spiking, peaks at approximately similar times across electrodes. In addition, we observed that the high-gamma amplitude peaks occur shortly after the transition time between consonant and vowels, which shows that the traveling waves are therefore entrained to the rhythm of speech production.

3 Discussion

We have shown that rhythmic speech production entrains low-frequency brain oscillations (Figure 1) and that this entrainment is stronger over the vSMC (Figure 2), that rhythmic speech production modulates the power of beta oscillations over the auditory cortex and that of high-gamma oscillations over the vSMC (Figure 3), that the phase of the entrained low-frequency oscillations couples with the amplitude of high-gamma oscillations (Figure 4) and that this coupling is largest over the vSMC (Figure A.44), that over the vSMC –but not over the auditory cortex– this coupling is maximal between phase at the entrained frequency and amplitude in the high-gamma range (Figure 5), and that the entrained oscillations organize as TWs synchronized to the produced speech (Figure 6 and movie at `https://youtu.be/dXrzj2eEuVY`). Finally, we observed that the peaks of PAC curves occur at earlier phases along the direction of propagation of the TWs and presented evidence (Figure 7) indicating that this organization of PAC curves enables neurons along the direction of

propagation of the TW to fire at the same behaviorally relevant time.

These initial findings open several interesting directions for future investigations. To mention a few: (1) How do entrainment, PAC, and TWs relate to properties of the produced CV syllables? For example, does PAC occur earlier for fricatives than for nasals? (2) How do these effects (i.e., entrainment, PAC, and TWs) correspond to the specific articulators recruited in the production of a CV syllable? For example, do planar TWs correspond to the recruitment of the jaw but rotating TWs to the recruitment of the larynx? (3) PAC has been reported in speech perception (e.g., Giraud and Poeppel, 2012; Hyafil et al., 2015), but not in speech production tasks. We claimed that the PAC we observed is related to speech production, but we have not eliminated the possibility that it may be related to the perception of the speaker's own speech. The detection of PAC in new experiments eliminating speech feedback would confirm that PAC can be related to the production of speech. (4) The observed effects appeared in the strongly rhythmic production of CV syllables. Would similar effects be observed in colloquial speech? How do prosodic features of speech, like intonation or stress, affect the observed effects? (5) We have characterized phase coherence and PAC at single electrodes, but probably phase coherence and PAC across different electrodes play an important role in the synchronization and information transfer across different speech perception and production brain regions, as observed in non-speech-processing tasks (e.g., Voytek et al., 2015).

It is possible to explain some of our results in terms of event-related potentials (ERPs, the mean recorded potential around an event of interest). Previous studies have suggested that ERPs are generated by the alignment of phases of ongoing oscillations (Makeig et al., 2002), but this suggestion is still controversial (Sauseng et al., 2007). Because the production of CV syllables occurred at a low-frequency rhythm, ERPs should be generated at this low-frequency and we should observe alignment of phases at this low frequency. Thus, this ERP argument explains Figure 1. Also, since ERPs should be stronger over the vSMC, we should expect more phase alignment over this region, explaining Figure 2. One could argue that the production of speech is related to spiking, and therefore to high-gamma activity, over the vSMC. Thus, the low frequency phase at which oscillations reset for the generation of ERPs should be related to high-gamma activity. This argument addresses Figures 4 and 5.

Section A.5 shows ERPs computed along the ventral-dorsal axis of the recording grid. In agreement with Figure 2, we see strongest ERPs at electrodes 136-140 over the vSMC. These ERPs begin around 150 msec before the CV transition, peak around 100 ms after this transition, and show a negative peak around 400 ms after the CV transition. Also, in agreement with Figure 4 we see that the peak of the ERPs are shifted to later times as we move from electrode 136 to electrode 140, also suggesting the existence of TWs.

Thus, the spectral and ERP analysis are consistent with each other. An advantage of the former is that it decomposes the averaged effects seen in ERPs in different frequency bands. Since several frequency-specific effects on electrophysiological recordings are known, spectral analysis allow richer descriptions

of electrophysiological recordings than ERP ones. For instance by decomposing averaged effects in different frequency bands, our spectral analysis showed that neural spiking, as reflected by high-gamma amplitude, was coupled to relevant times in the speech production rhythm, as indicated by the coupled phase at the speech-production frequency (Figure 4). Also, our PAC analysis is more quantitative than the previous argument linking ERPs and high-gamma amplitude. This analysis revealed a new organization of PAC in the presence of TWs, providing strong support to a previous hypothesis stating that, when stimuli or behavior occurs in a rhythmic fashion, PAC is a mechanism that allows neurons to spike at behavioral relevant times (Canolty and Knight, 2010). In summary, the spectral methods used above to characterize rhythmic speech production are consistent with, but superior than, ERP methods for the characterization of rhythmic behaviors such as speech.

The effects reported above reflect brain mechanisms beyond the control of vocal articulators. For example, the traveling wave movie (`https://youtu.be/dXrzj2eEuVY`) shows waves moving across multiple speech processing brain regions. At several times we see waves moving from electrodes over the auditory cortex to electrodes over the vSMC, suggesting that these waves could be a mechanism for integrating information across the brain, as suggested by others (e.g., Nunez and Srinivasan, 2006; Sato et al., 2012).

As speaking must be compatible with the performance limits of motor systems, several theories have linked functional properties of motor systems to speech capability. The Frame/Content theory (MacNeilage and Davis, 2000, 2001) proposes that the features of elementary production units, i.e., syllables, are determined by mechanical properties of the speech apparatus, e.g., natural oscillatory rhythms (Giraud et al., 2007). Previous investigations (e.g., Morillon et al., 2010) have hypothesized that motor areas express low-frequency oscillatory activity characteristic of jaw movements (4 Hz) and high-frequency activity corresponding to movements of the tongue (e.g., trill at 35-40 Hz). However, to our knowledge this is the first study providing physiological evidence for the relation of low- and high-frequency oscillations, as well as their interactions, to speech production.

Natural speech production is substantially more complex than the production of CV syllables, which suggests that the findings reported in this article may not be relevant to natural speech. We argue on the contrary. CV syllables are the building blocks of natural speech, such as sinusoidal grating are the building blocks of natural images. While producing CV syllables subjects spontaneously enter a strongly rhythmic behavioral state. Natural speech is strongly rhythmic and the production of CV syllables could be ideal to isolate rhythmic aspects of this behavior. By characterizing responses of visual cells to sinusoidal gratings, it has been possible to understand key neural mechanisms of visual processing, like contrast grain control (Ohzawa et al., 1985), that are difficult to observe in responses of visual neurons to complex natural images. Similarly, investigating the production of CV syllables may be instrumental in discovering key rhythmic mechanisms of speech production that are obscured in more complex speech-production tasks.

The specific attributes of mesoscopic cortical activity related to speech production are not well characterized. In speech perception, Luo and Poeppel (2007) have shown that phase activity (over the human auditory cortex in the theta range (4-8 Hz) recorded with MEG) reliably tracks and discriminates spoken sentences and that this discrimination is correlated with speech intelligibility. Here we extended these results and showed that phase activity (in the form of phase alignment, PAC, and TWs) is also a relevant mesoscopic attribute to characterize the neurophysiology of speech production.

Having detected phase alignment, PAC and TWs in ECoG recordings, one could use forward models to calculate how these effects propagate to scalp-recorded potentials in the EEG or magnetic fields in the MEG. Next, one could invert these forward models to infer the existence and properties of these oscillatory effects from EEG or MEG recordings (Friston et al., 2007). If successful this approach would allow to detect phase alignment, PAC, and TWs from non-invasive recordings, and provide novel measures to non-invasively characterize speech production in health and disease.

4 Acknowledgments

We thank Dr. Edward Chang and Dr. Kristofer Bouchard for sharing the ECoG recordings with us and for comments on a preliminary version of this manuscript, and Dr. John Iversen for suggesting us the relation between PAC and TWs.

References

E.D. Adrian and B.H.C. Matthews. The berger rhythm : potential changes from the occipital lobes in man. *Brain*, 57(4):355–385, 1934.

Ali Bahramisharif, Marcel AJ van Gerven, Erik J Aarnoutse, Manuel R Mercier, Theodore H Schwartz, John J Foxe, Nick F Ramsey, and Ole Jensen. Propagating neocortical gamma bursts are coordinated by traveling alpha waves. *The Journal of Neuroscience*, 33(48):18849–18854, 2013.

J. Besle, C.A. Schevon, A.D. Mehta, P. Lakatos, R.R. Goodman, G.M. McKhann, R.G. Emerson, and C.E. Schroeder. Tuning of the human neocortex to the temporal dynamics of attended events. *The Journal of Neuroscience*, 31(9):3176–3185, 2011.

R.T. Canolty and R.T. Knight. The functional role of cross-frequency coupling. *Trends in cognitive sciences*, 14(11):506–515, 2010.

R.T. Canolty, E. Edwards, S.S. Dalal, M. Soltani, S.S. Nagarajan, H.E. Kirsch, M.S. Berger, N.M. Barbaro, and R.T. Knight. High gamma power is phase-locked to theta oscillations in human neocortex. *science*, 313(5793):1626–1628, 2006.

A.M. Cravo, G. Rohenkohl, V. Wyart, and A.C. Nobre. Temporal expectation enhances contrast sensitivity by phase entrainment of low-frequency oscillations in visual cortex. *Journal of Neuroscience*, 33(9):4002–4010, 2013.

F. Cummins. Oscillators and syllables: a cautionary note. *Frontiers in psychology*, 3: 364, 2012.

A. Delorme and S. Makeig. EEGLAB: an open source toolbox for analysis of single-trial EEG dynamics including independent component analsys. *Journal of Neuroscience Methods*, 134(1):9–21, 2004.

N. Ding and J.Z. Simon. Cortical entrainment to continuous speech: functional roles and interpretations. *Front. Hum. Neurosci*, 8(311):10–3389, 2014.

Keith B Doelling, Luc H Arnal, Oded Ghitza, and David Poeppel. Acoustic landmarks drive delta–theta oscillations to enable speech comprehension by facilitating perceptual parsing. *Neuroimage*, 85:761–768, 2014.

K.J. Friston, J.T. Ashburner, S.J. Kiebel, T.E. Nichols, and W.D. Penny, editors. *Statistical Parametric Mapping*. Academic Press, London, 2007.

Robert Galambos, Scott Makeig, and Peter J Talmachoff. A 40-hz auditory potential recorded from the human scalp. *Proceedings of the National Academy of Sciences*, 78(4):2643–2647, 1981.

A.L. Giraud, A. Kleinschmidt, D. Poeppel, T.E. Lund, R.S.J. Frackowiak, and H. Laufs. Endogenous cortical rhythms determine cerebral specialization for speech perception and production. *Neuron*, 56(6):1127–1134, 2007.

Anne-Lise Giraud and David Poeppel. Cortical oscillations and speech processing: emerging computational principles and operations. *Nature neuroscience*, 15(4):511–517, 2012.

M. Gomez-Ramirez, S.P. Kelly, S. Molholm, P Sehatpour, T.H. Schwartz, and J.J. Foxe. Oscillatory sensory selection mechanism during intersensory attention to rhythmic auditory and visual inputs: a human electrocortigraphic investigation. *The Journal of Neuroscience*, 31(50):18556–18567, 2011.

Michael J Gray, Hans-Peter Frey, Tommy J Wilson, and John J Foxe. Oscillatory recruitment of bilateral visual cortex during spatial attention to competing rhythmic inputs. *The Journal of Neuroscience*, 35(14):5489–5503, 2015.

J. Gross, N. Hoogenboom, G. Thut, P. Schyns, S. Panzeri, P. Belin, and S. Garrod. Speech rhythms and multiplexed oscillatory sensory coding in the human brain. *PLoS Biology*, 11(12), 2013. doi: 10.1371/journal.pbio.1001752.

A. Hyafil, L. Fontolan, C. Kabdebon, B. Gutkin, and A.L. Giraud. Speech encoding by coupled cortical theta and gamma oscillations. *Elife*, 4:e06213, 2015.

P. Lakatos, A.S. Shah, K.H. Knuth, I. Ulbert, G. Kamos, and C.E. Schroeder. An oscillatory hierarchy controlling neural excitability and stimulus processing in the auditory cortex. *J. Neurophysiology*, 94(3):1904–1911, 2005.

P. Lakatos, G. Karmos, A.D. Mehta, I. Ulbert, and C.E. Schroeder. Entrainment of neuronal oscillations as a mechanism of attentional selection. *Science*, 320:110–113, 2008.

P. Lakatos, G. Musacchia, M.N. O'connel, A.Y. Falchier, D.C. Javitt, and C.E. Schroeder. The spectrotemporal filter mechanism of auditory selective attention. *Neuron*, 77(4):750–761, 2013.

Huan Luo and David Poeppel. Phase patterns of neuronal responses reliably discriminate speech in human auditory cortex. *Neuron*, 54(6):1001–1010, 2007.

P.F. MacNeilage and B.L. Davis. On the origin of internal structure of word forms. *Science*, 288(5465):527–531, 2000.

P.F. MacNeilage and B.L. Davis. Motor mechanisms in speech ontogeny: phylogenetic, neurobiological and linguistic implications. *Current opinion in neurobiology*, 11(6): 696–700, 2001.

S. Makeig, M. Westerfield, T.P. Jung, S. Enghoff, J. Townsend, E. Couchesne, and T.J. Sejnowski. Dynamic brain sources of visual evoked responses. *Science*, 295 (5555):690–694, 2002.

K.V. Mardia. *Statistics of directional data*. Acadmic Press, New York, NY, 1972.

K.E. Mathewson, M. Fabiani, G. Gratton, D.M. Beck, and A. Lleras. Rescuing stimuli from invisibility: Inducing a momentary release from visual masking with pre-target entrainment. *Cognition*, 115:186–191, 2010.

R.E. Millman, S.R. Johnson, and G. Prendergast. The role of phase-locking to the temporal envelope of speech in auditory perception and speech intelligibility. *Journal of cognitive neuroscience*, 2015.

B. Morillon, K. Lehongre, R.S.J. Frackowiak, A. Ducorps, A. Kleinschmidt, D. Poeppel, and A.L. Giraud. Neurophysiological origin of human brain asymmetry for speech and language. *Proceedings of the National Academy of Sciences*, 107(43): 18688–18693, 2010.

P.L. Nunez and R. Srinivasan. A theoretical basis for standing and traveling brain waves measured with human eeg with implications for an integrated consciousness. *Clinical Neurophysiology*, 117(11):2424–2435, 2006.

M.N. O'Connell, A. Falchier, T. McGinnis, C.E. Schroeder, and P. Lakatos. Dual mechanism of neuronal ensemble inhibition in primary auditory cortex. *Neuron*, 69 (4):805–817, 2011.

I. Ohzawa, G. Sclar, and R.D. Freeman. Contrast gain control in the cat's visual system. *Journal of Neurophysiology*, 54(3):651–667, 1985.

Hyojin Park, Robin AA Ince, Philippe G Schyns, Gregor Thut, and Joachim Gross. Frontal top-down signals increase coupling of auditory low-frequency oscillations to continuous speech in human listeners. *Current Biology*, 2015.

Timothy M Patten, Christopher J Rennie, Peter A Robinson, and Pulin Gong. Human cortical traveling waves: dynamical properties and correlations with responses. *PLoS One*, 7(6):e38392, 2012.

J.E. Peelle and M.H. Davis. Neural oscillations carry speech rhythm through to comprehension. *Front Psychol*, 3(320):1–17, 2012.

S. Ray, N.E. Crone, . Niebur, P.J Franaszczuk, and S.S. Hsiao. Neural correlates of high-gamma oscillations (60–200 hz) in macaque local field potentials and their potential implications in electrocorticography. *The Journal of Neuroscience*, 28(45): 11526–36, 2008.

D Regan. Some characteristics of average steady-state and transient responses evoked by modulated light. *Electroencephalography and clinical neurophysiology*, 20(3):238–248, 1966.

D. Rubino, K.A. Robbins, and N.G. Hatsopoulos. Propagating waves mediate information transfer in the motor cortex. *Nature neuroscience*, 9(12):1549–1557, 2006.

T.K. Sato, I. Nauhaus, and M. Carandini. Traveling waves in visual cortex. *Neuron*, 75(2):218–229, 2012.

P. Sauseng, W. Klimesch, W.R. Gruber, S. Hanslmayr, R. Freunberger, and M. Doppelmayr. Are event-related potential components generated by phase resetting of brain oscillations? a critical discussion. *Neuroscience*, 146(4):1435–1444, 2007.

C.E. Schroeder and P. Lakatos. Low-frequency neuronal oscillations as instruments of sensory selection. *Trends in Neurosciences*, 32(1):9–18, 2009.

E. Spaak, F.P. de Lange, and O Jensen. Local entrainment of alpha oscillations by visual stimuli causes cyclic modulation of perception. *J Neurosci*, 34(10):3536–44, 2014.

C. Tallon Baudry, O. Bertrand, C. Delpuech, and J. Pernier. Stimulus specificity of phase-locked and non-phase-locked 40 hz visual responses in human. *Journal of Neuroscience*, 16:4240–4349, 1996.

Adriano BL Tort, Robert Komorowski, Howard Eichenbaum, and Nancy Kopell. Measuring phase-amplitude coupling between neuronal oscillations of different frequencies. *Journal of neurophysiology*, 104(2):1195–1210, 2010.

Bradley Voytek, Andrew S Kayser, David Badre, David Fegen, Edward F Chang, Nathan E Crone, Josef Parvizi, Robert T Knight, and Mark D'Esposito. Oscillatory dynamics coordinating human frontal networks in support of goal maintenance. *Nature neuroscience*, 2015.

E.M. Zion Golumbic, D. Poeppel, and C.E. Schroeder. Temporal context in speech processing and attentional stream selection: a behavioral and neural perspective. *Brain and language*, 122(3):151–161, 2012.

E.M. Zion Golumbic, N. Ding, S. Bickel, P. Lakatos, C.A. Schevon, G.M. McKhann, R.R. Goodman, R. Emerson, A.D. Mehta, J.Z. Simon, D. Poeppel, and C.E. Schroeder. Mechanisms underlying selective neuronal tracking of attended speech at a "cocktail party". *Neuron*, 77(5):980–991, 2013.

E.M. Zion Golumbic, N. Ding, S. Bickel, P. Lakatos, C.A. Schevon, G.M. McKhann, R.R. Goodman, R. Emerson, A.D. Mehta, J.Z. Simon, D. Poeppel, and C.E. Schroeder. Mechanisms underlying selective neuronal tracking of attended speech at a cocktail party. *Neuron*, 77(5):980–991, 2013.

A Supplementary Information

A.1 Methods

A.1.1 Circular statistics concepts

This section introduces concepts from circular statistics (Mardia, 1972) used below to define ITC. Given a set of circular variables (e.g., phases), $\theta_1, \ldots, \theta_N$, we associate to each circular variable a two-dimensional unit vector. Using notation from complex numbers, the unit vector associated with variable θ_i is:

$$vec(\theta_i) = e^{j\theta_i} \tag{1}$$

The *resultant vector*, $\mathbf{R}$, is the sum of the associated unit vectors:

$$\mathbf{R}(\theta_1, \ldots, \theta_N) = \sum_{i=1}^{N} vec(\theta_i) \tag{2}$$

The *mean resultant length*, $\bar{R}$, is the length of the resultant vector divided by the number of variables:

$$\bar{R}(\theta_1, \ldots, \theta_N) = \frac{1}{N}|\mathbf{R}(\theta_1, \ldots, \theta_N)| \tag{3}$$

The *circular variance*, CV, is one minus the mean resultant length:

$$CV(\theta_1, \ldots, \theta_N) = 1 - \bar{R}(\theta_1, \ldots, \theta_N) \tag{4}$$

The *mean direction*, $\bar{\theta}$, is the angle of the resultant vector:

$$\bar{\theta}(\theta_1, \ldots, \theta_N) = \arg(\mathbf{R}(\theta_1, \ldots, \theta_N)) \tag{5}$$

Note that the mean direction is not defined when the resultant vector is zero, since the angle of the zero vector is undefined.

A.1.2 ITC

The Inter-Trial Coherence (ITC) is a measure of phase alignment among multiple trials at a given time and frequency (Tallon Baudry et al., 1996; Delorme and Makeig, 2004). Mathematically, it is defined as the mean resultant length ($\bar{R}$, Eq. 3) of the phases of the trials at the given time and frequency.

A.1.3 ERSP

The Event-Related Spectral Perturbation (ERSP) is the mean power of a set of baseline-normalized epochs (Delorme and Makeig, 2004).

A.1.4 Phase-amplitude coupling curve and modulation index

The PAC curve is a graphical means of representing the coupling between phases at a modulating frequency and amplitudes at a modulated frequency. The MI is a numerical quantification of the strength of this coupling. We used the methods described in Tort et al. (2010) to compute both the PAC curve and the MI.

A.2 Behavioral Data

Subjects produced consonant-vowel syllables at different speeds in different experimental sessions. This manuscript characterizes data in the experimental sessions with largest and shortest median intersyllable separation times (Figure A.1).

A.3 ITC across the vSMC

Largest coherence values at the entrained frequency were observed over the vSMC. Figures A.2-A.17 plot the ITC, computed from recordings in experimental session EC2_B105, between the ventral electrode 129 and the dorsal electrode 144. For electrodes over the temporal cortex there is almost no ITC (Figures A.2-A.4). ITC increases over the ventral section of the vSMC (Figures A.5-A.8), peaks at its center (Figures A.9-A.12), and tapers over its dorsal section (Figures A.13-A.17).

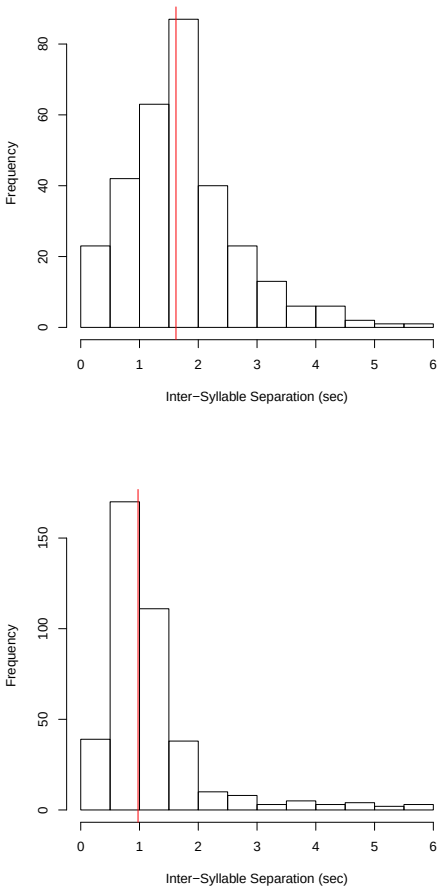

Figure A.1: Histogram of inter-syllable separations from the experimental sessions with the largest (1.62 sec) and shortest (0.97 sec) intersyllable separation time, EC2_B105 (a) and EC2_B89 (b), respectively.

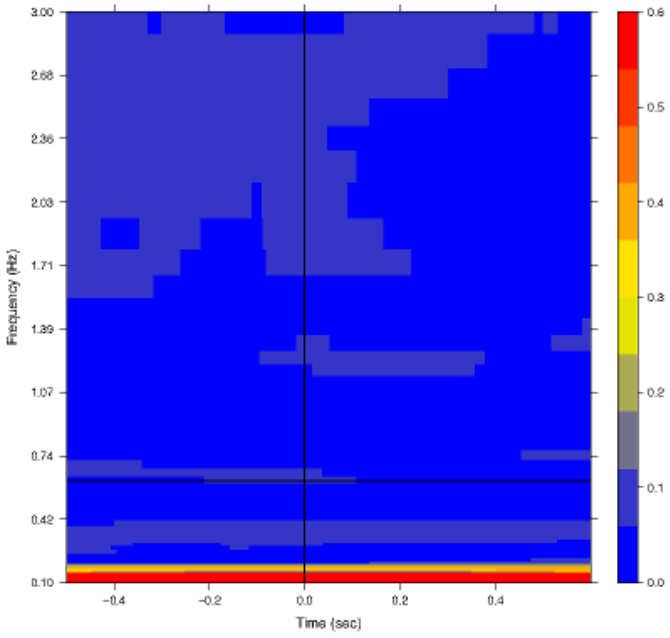

Figure A.2: ITC for electrode 129 computed from recordings in experimental session EC2_B105.

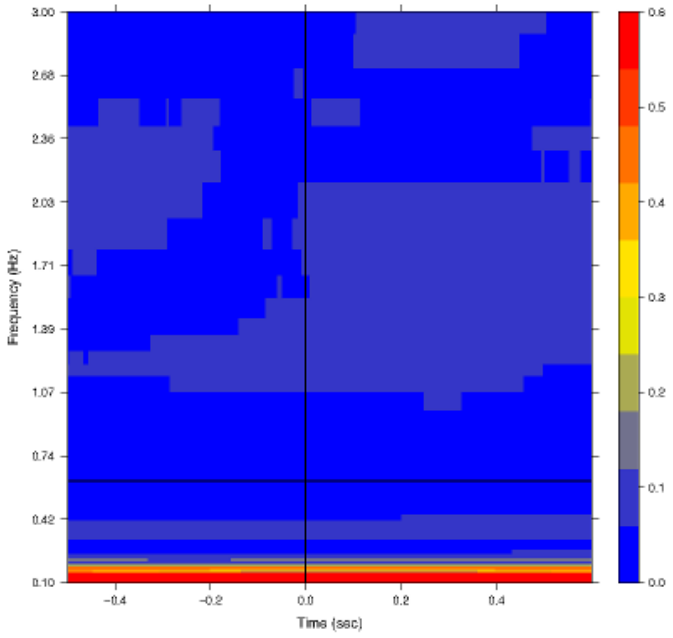

Figure A.3: ITC for electrode 130 computed from recordings in experimental session EC2_B105.

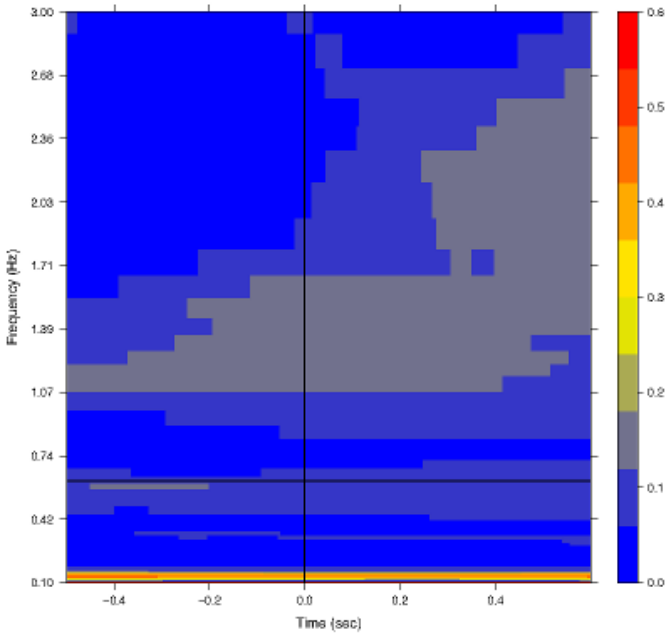

Figure A.4: ITC for electrode 131 computed from recordings in experimental session EC2_B105.

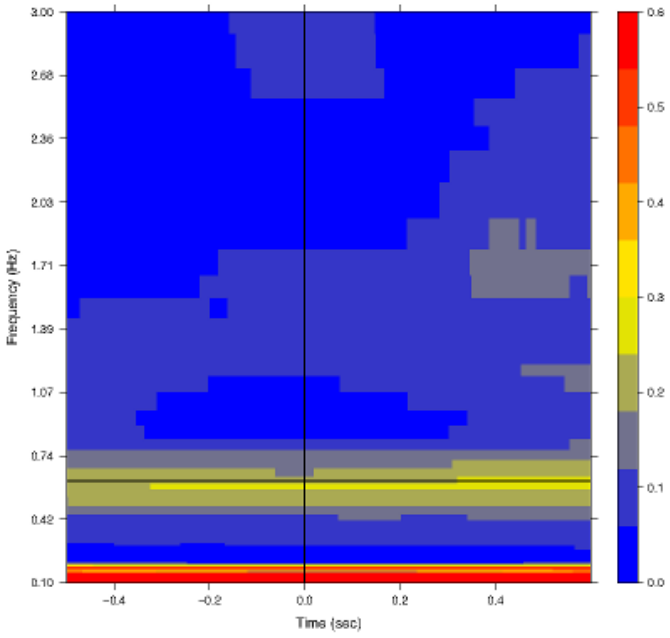

Figure A.5: ITC for electrode 132 computed from recordings in experimental session EC2_B105.

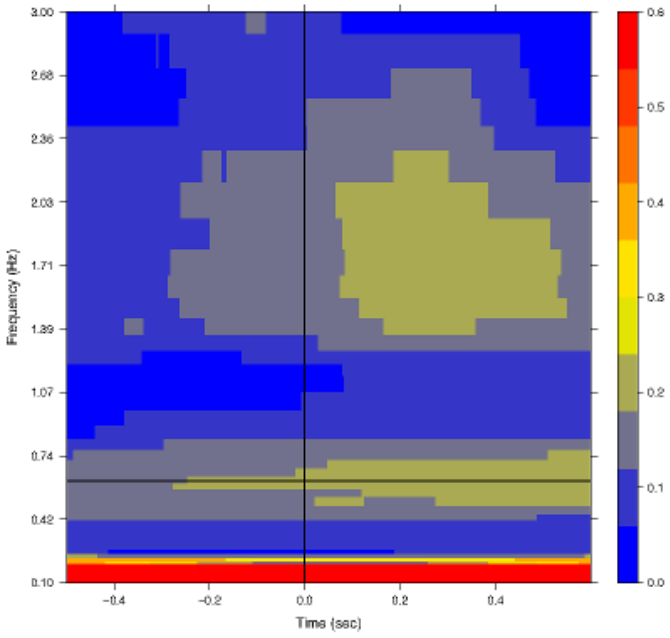

Figure A.6: ITC for electrode 133 computed from recordings in experimental session EC2_B105.

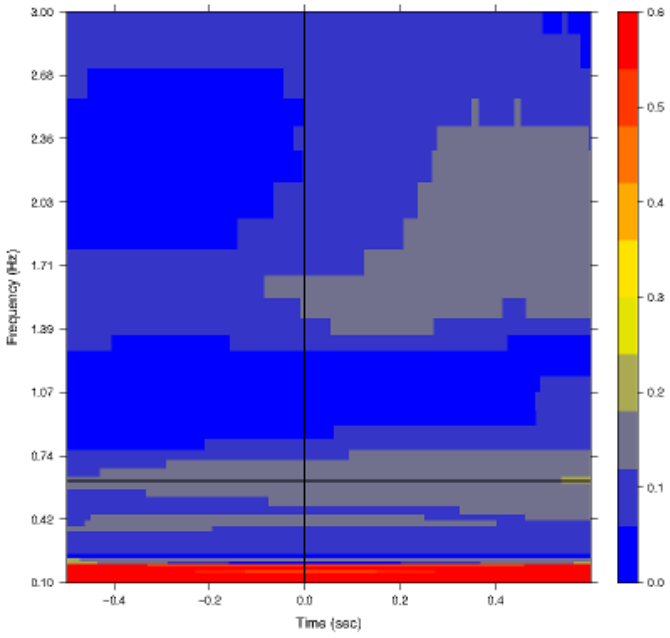

Figure A.7: ITC for electrode 134 computed from recordings in experimental session EC2_B105.

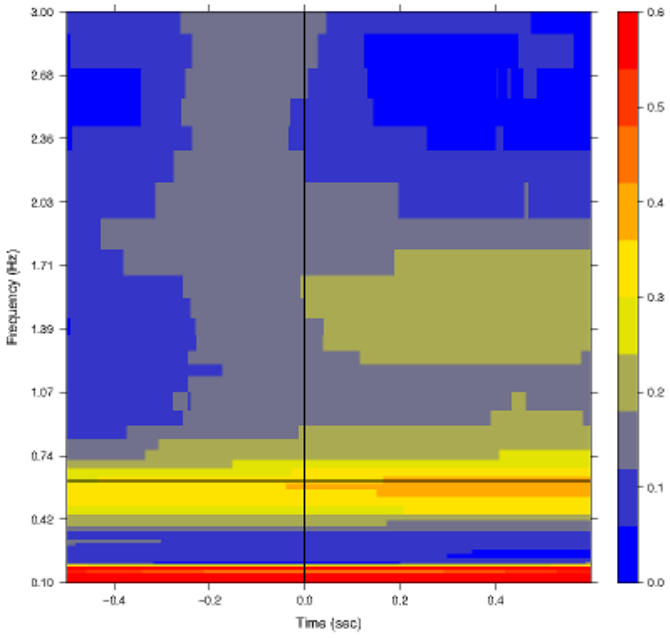

Figure A.8: ITC for electrode 135 computed from recordings in experimental session EC2_B105.

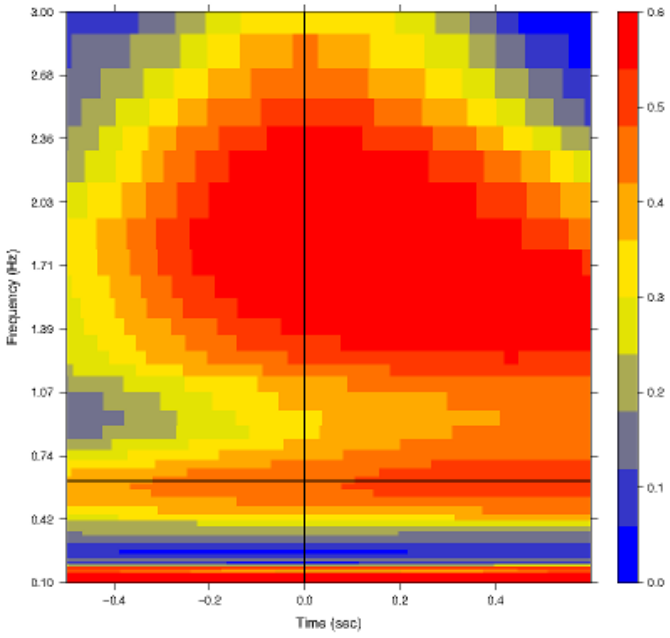

Figure A.9: ITC for electrode 136 computed from recordings in experimental session EC2_B105.

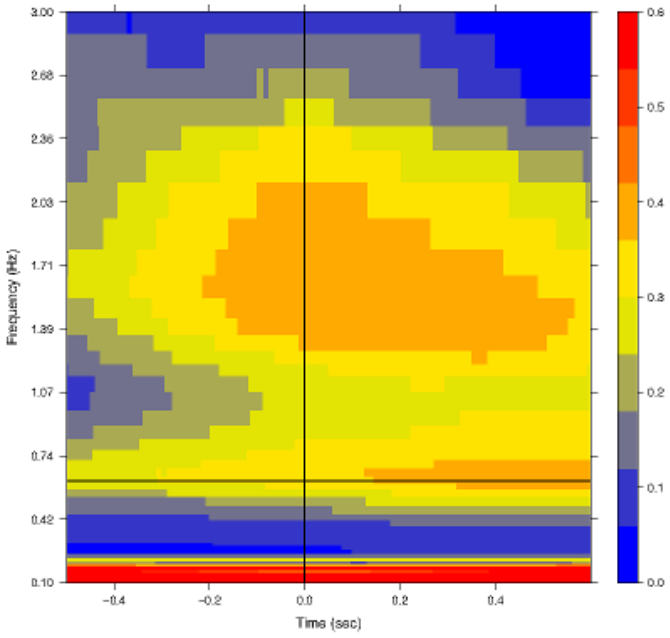

Figure A.10: ITC for electrode 137 computed from recordings in experimental session EC2_B105.

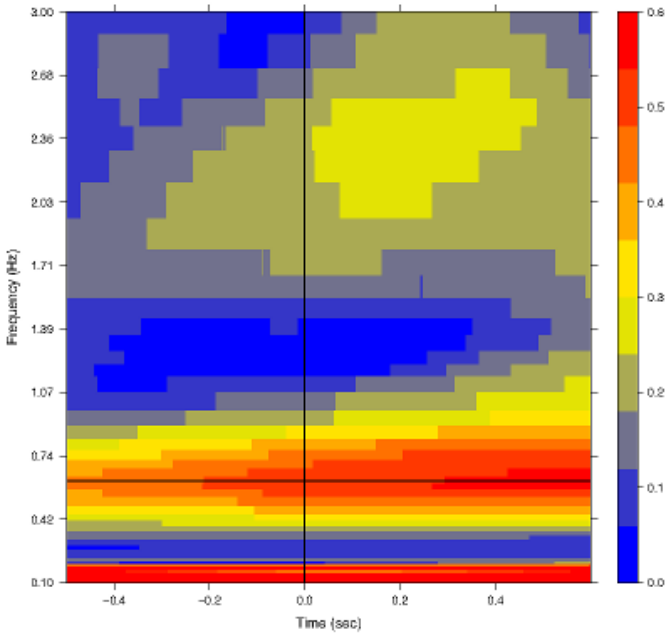

Figure A.11: ITC for electrode 138 computed from recordings in experimental session EC2_B105.

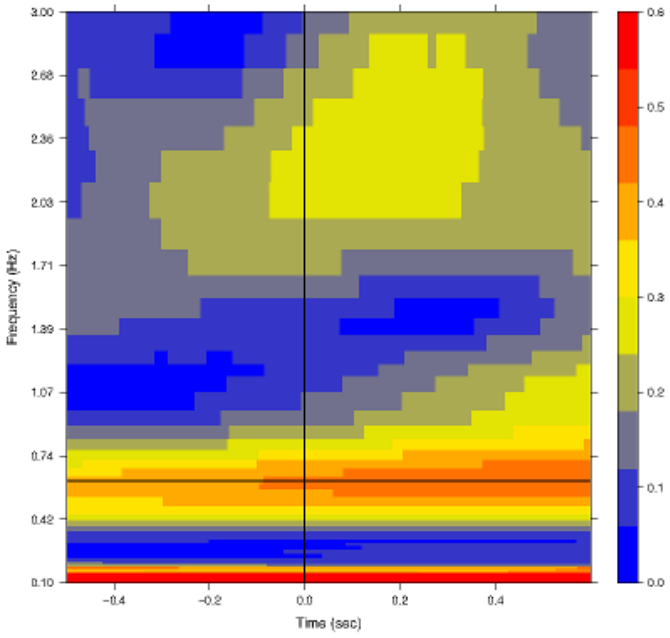

Figure A.12: ITC for electrode 139 computed from recordings in experimental session EC2_B105.

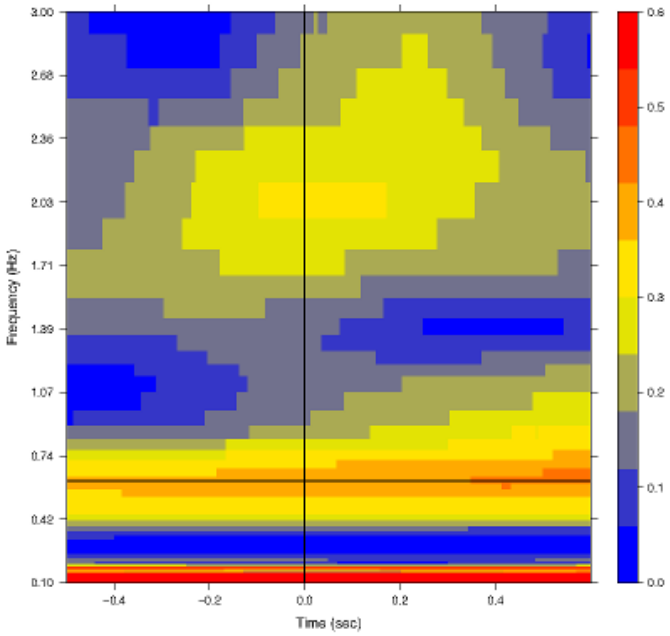

Figure A.13: ITC for electrode 140 computed from recordings in experimental session EC2_B105.

A.4 ERSPs across the vSMC

Figures A.18-A.30 plot ERSPs at electrodes along the ventro-dorsal axis of the vSMC. Note the sharp transition between the peak of large evoked beta power before the CV transition at electrodes 132-135 over the auditory cortex to the peak of large evoked high-gamma power after the CV transition at electrodes 135-140 over the vSMC.

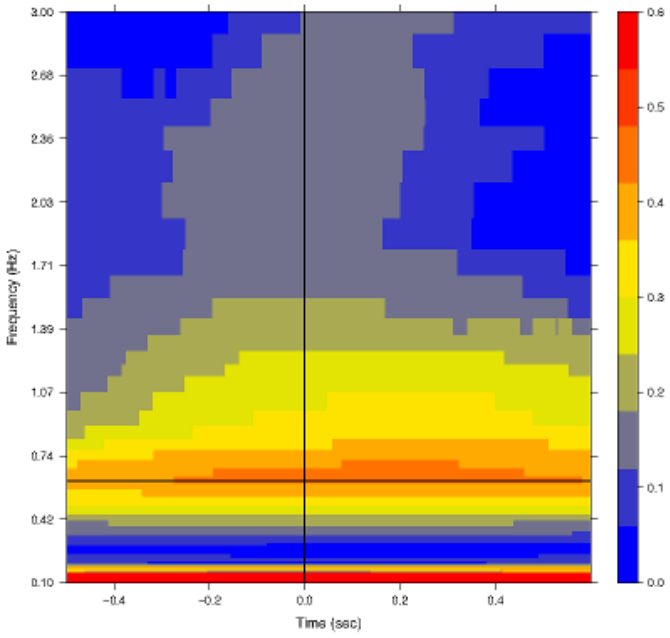

Figure A.14: ITC for electrode 141 computed from recordings in experimental session EC2_B105.

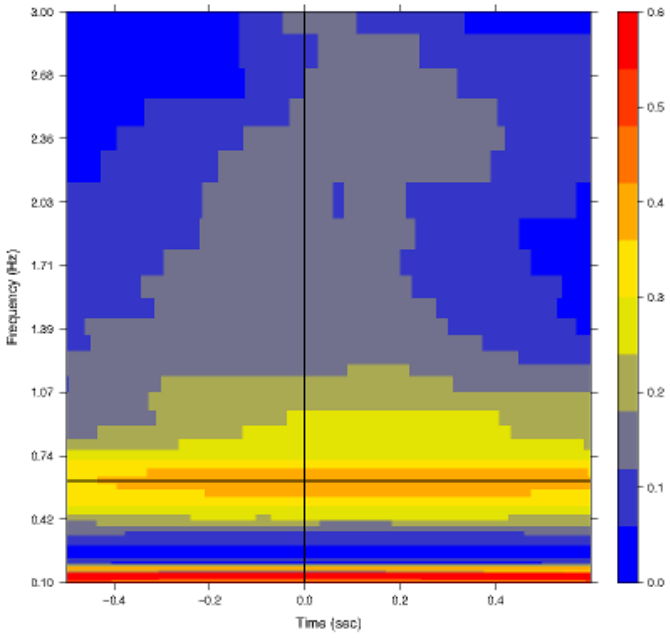

Figure A.15: ITC for electrode 142 computed from recordings in experimental session EC2_B105.

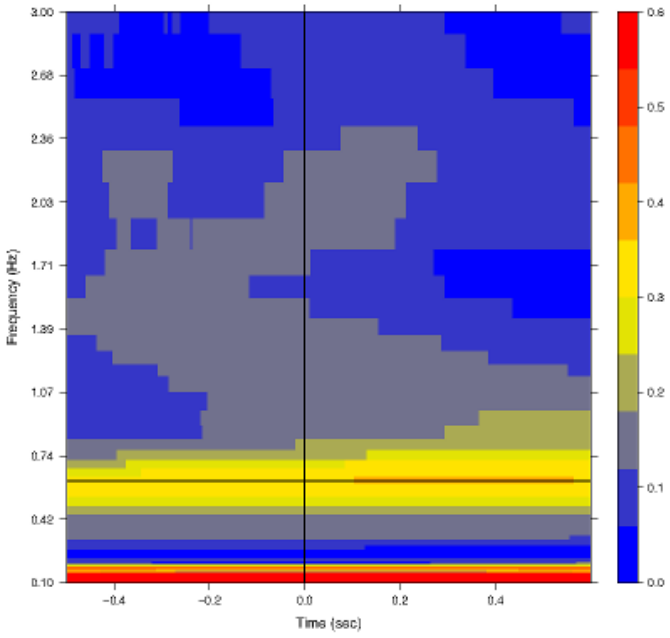

Figure A.16: ITC for electrode 143 computed from recordings in experimental session EC2_B105.

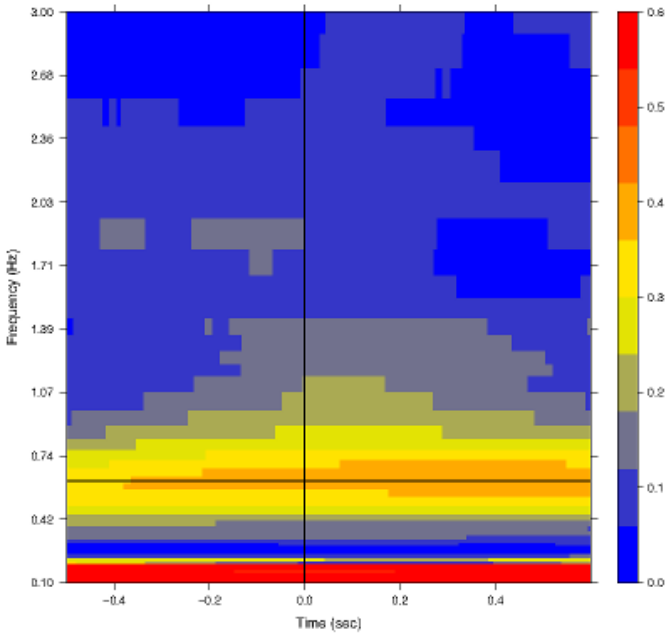

Figure A.17: ITC for electrode 144 computed from recordings in experimental session EC2_B105.

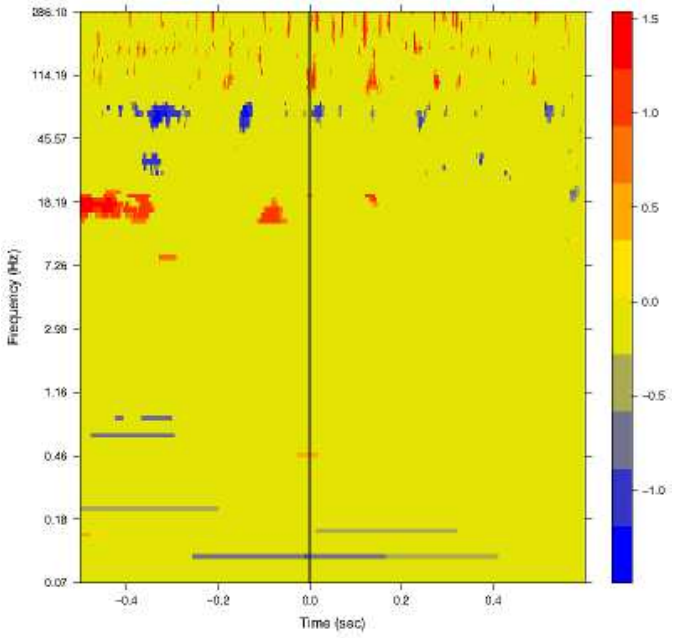

Figure A.18: ERSP for electrode 129 computed from recordings in experimental session EC2_B105.

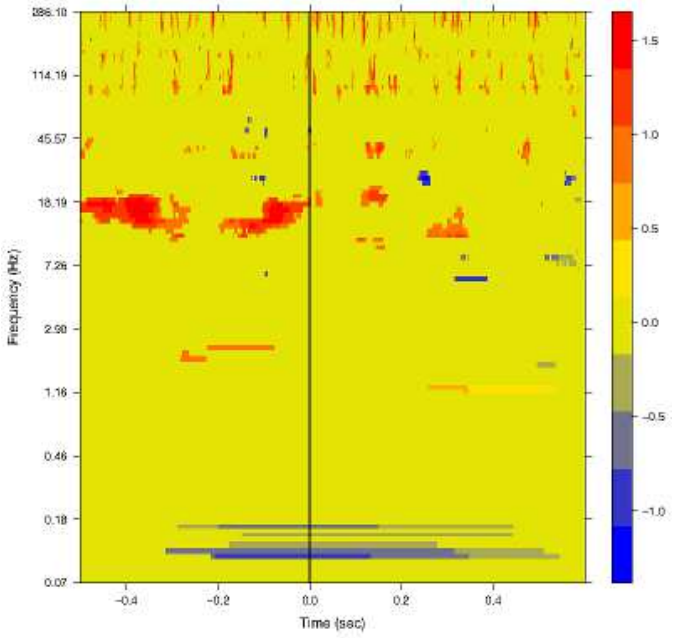

Figure A.19: ERSP for electrode 130 computed from recordings in experimental session EC2_B105.

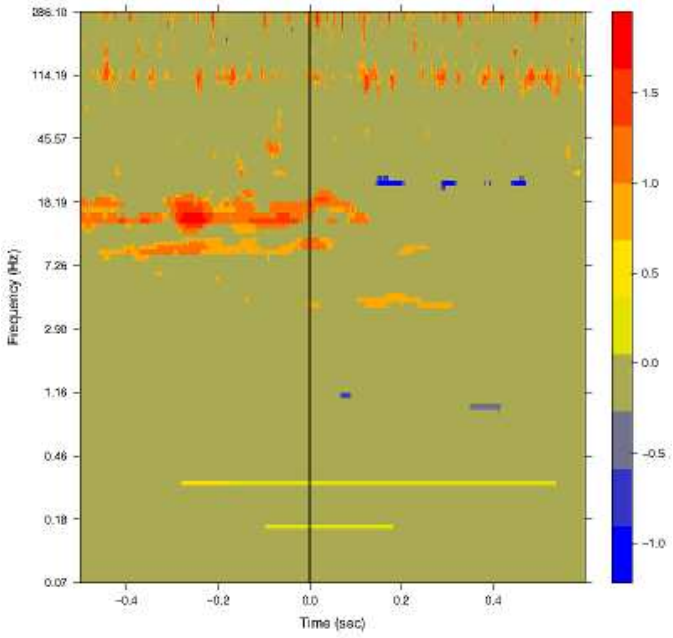

Figure A.20: ERSP for electrode 131 computed from recordings in experimental session EC2_B105.

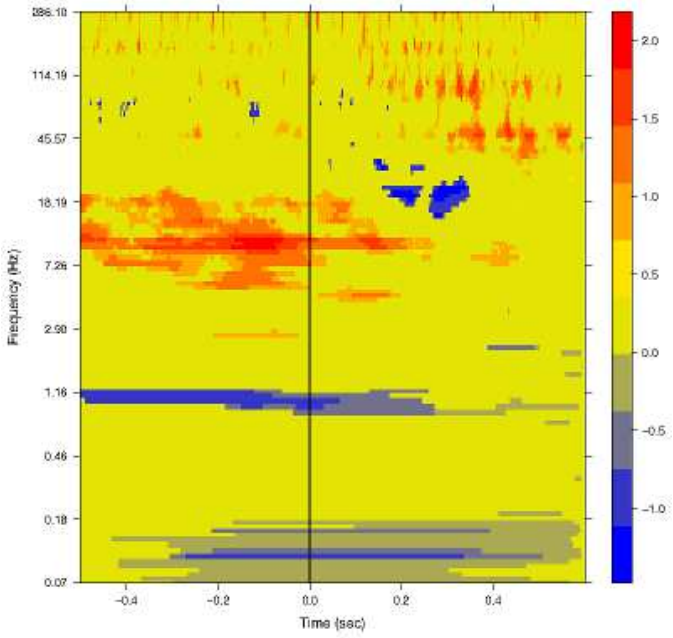

Figure A.21: ERSP for electrode 132 computed from recordings in experimental session EC2_B105.

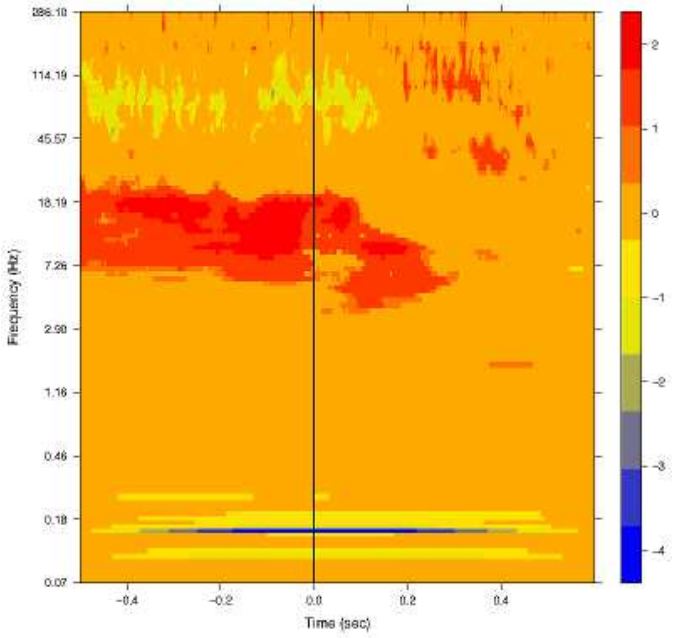

Figure A.22: ERSP for electrode 133 computed from recordings in experimental session EC2_B105.

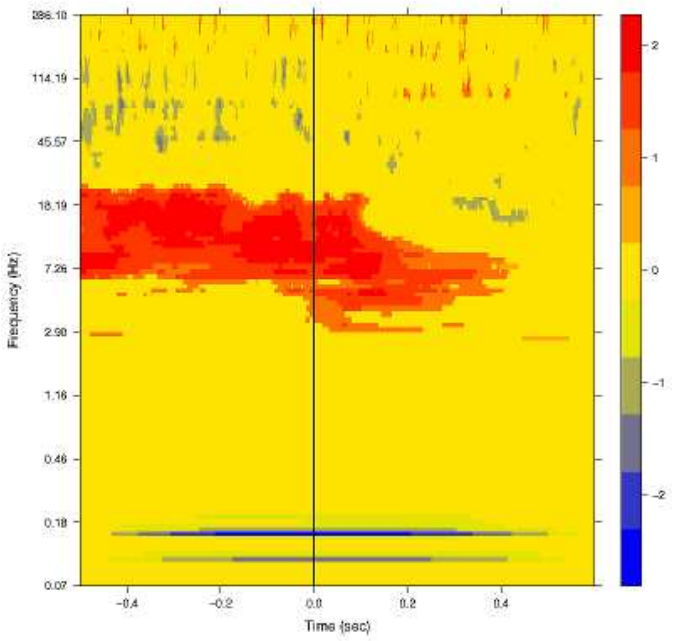

Figure A.23: ERSP for electrode 134 computed from recordings in experimental session EC2_B105.

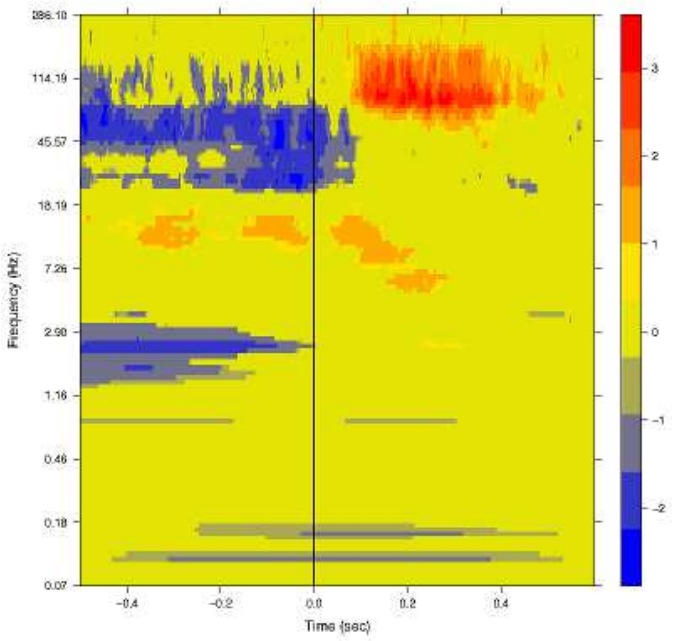

Figure A.24: ERSP for electrode 135 computed from recordings in experimental session EC2_B105.

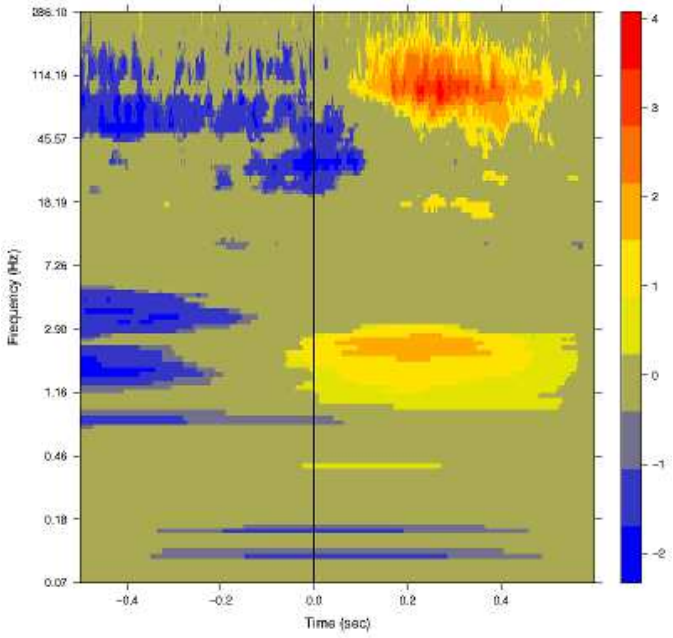

Figure A.25: ERSP for electrode 136 computed from recordings in experimental session EC2_B105.

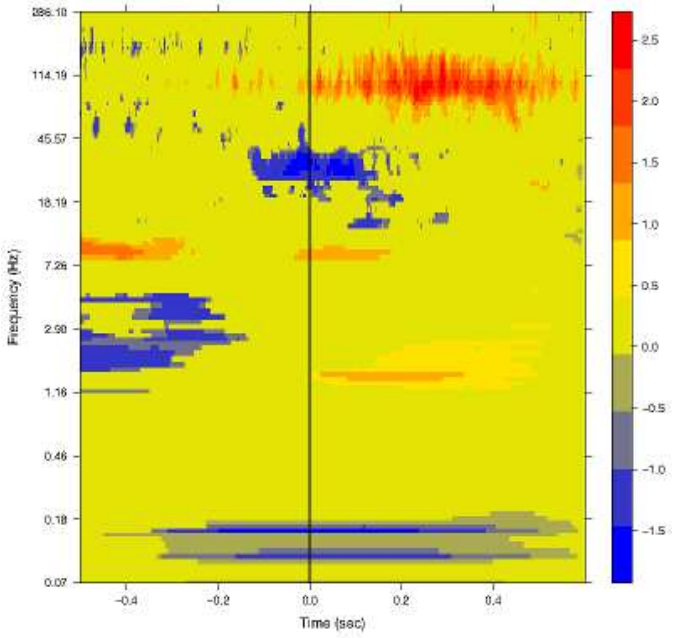

Figure A.26: ERSP for electrode 137 computed from recordings in experimental session EC2_B105.

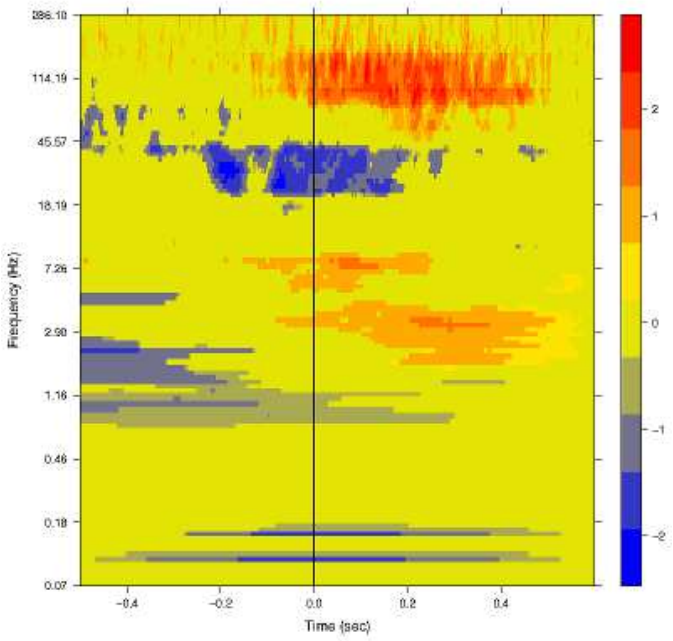

Figure A.27: ERSP for electrode 138 computed from recordings in experimental session EC2_B105.

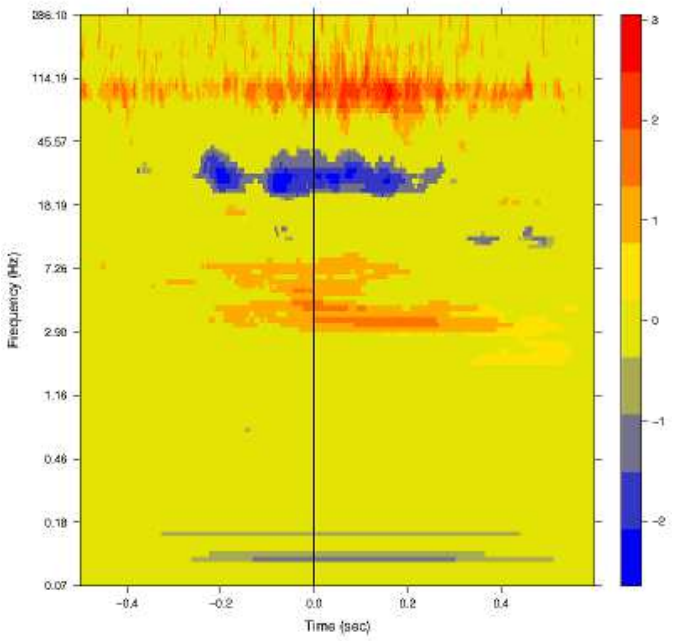

Figure A.28: ERSP for electrode 139 computed from recordings in experimental session EC2_B105.

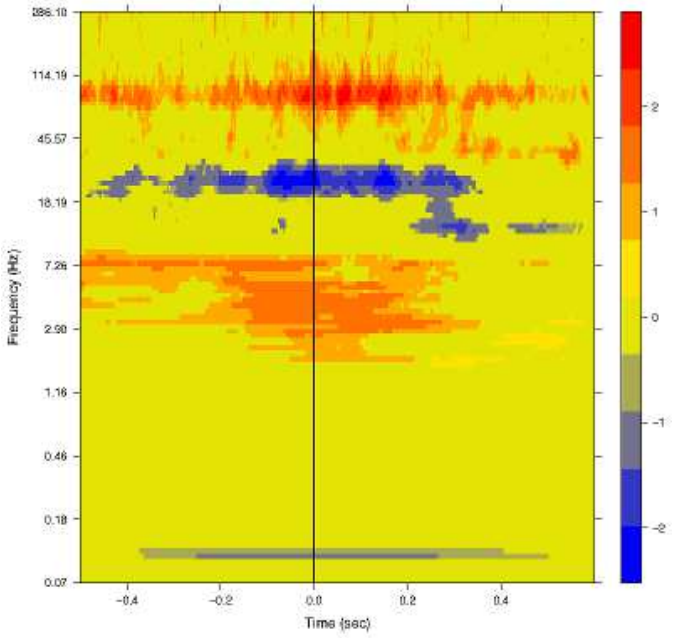

Figure A.29: ERSP for electrode 140 computed from recordings in experimental session EC2_B105.

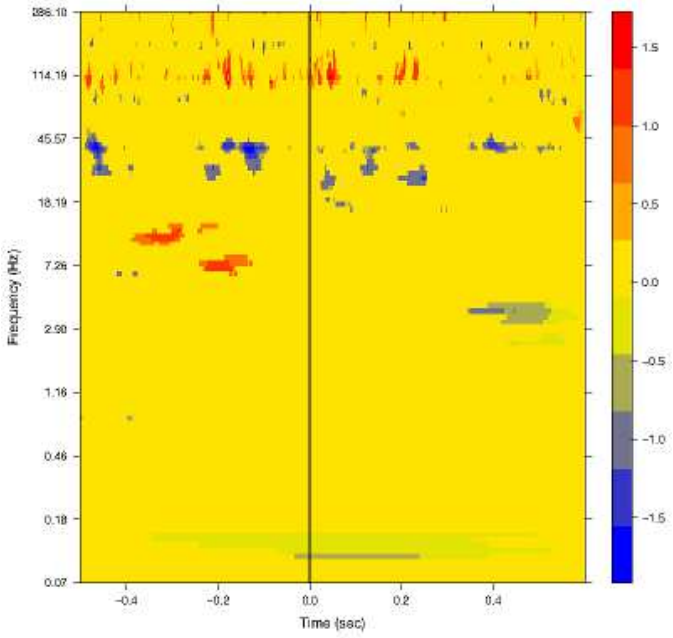

Figure A.30: ERSP for electrode 141 computed from recordings in experimental session EC2_B105.

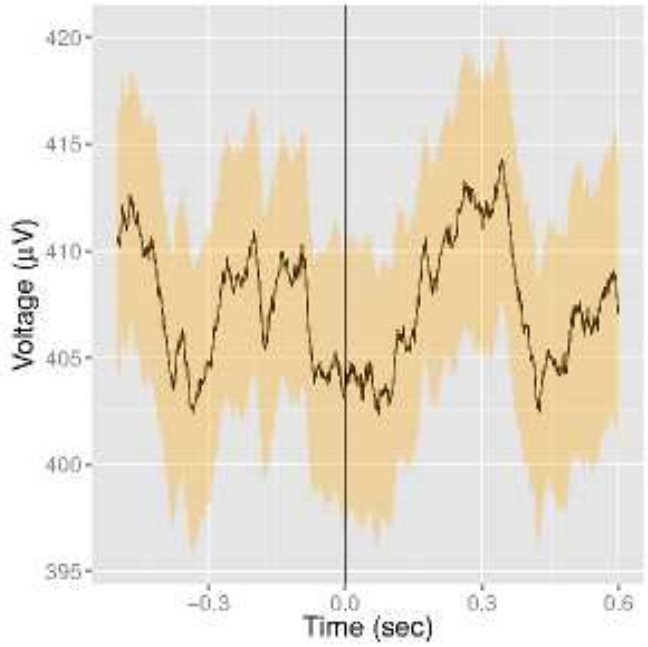

Figure A.31: ERP for electrode 129 computed from recordings in experimental session EC2_B105.

A.5 ERPs across the vSMC

Figures A.31-A.43 plots ERPs computed at electrodes along the ventro-dorsal axis of the recordings grid. Note that ERPs are larger over electrodes 136-140 in the vSMC, in agreement with Figure 2, and that the ERP peak is shifted to later times as we move from electrode 136 to electrode 140.

A.6 Electrodes with strongest PAC

Figure A.44 highlights the 50 electrodes with largest MI.

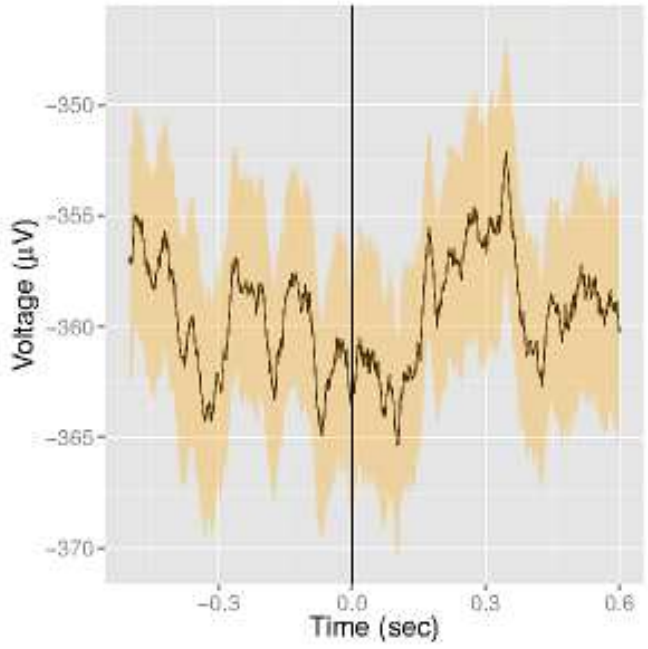

Figure A.32: ERP for electrode 130 computed from recordings in experimental session EC2_B105.

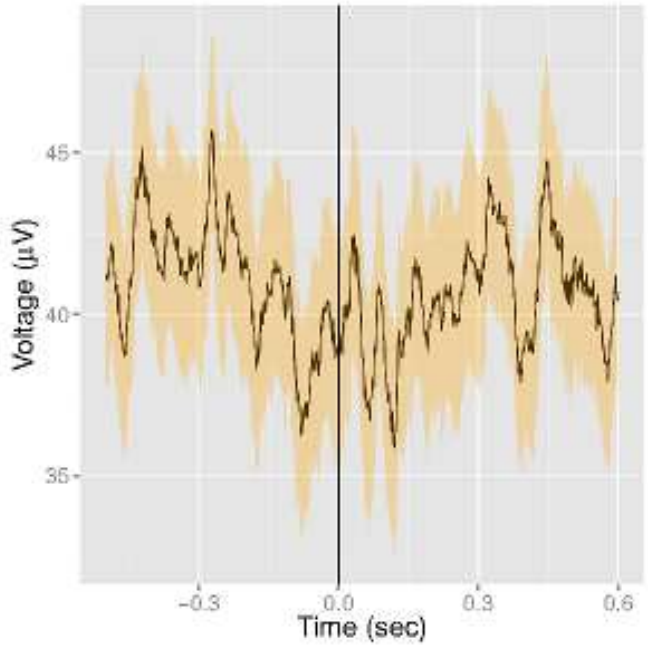

Figure A.33: ERP for electrode 131 computed from recordings in experimental session EC2_B105.

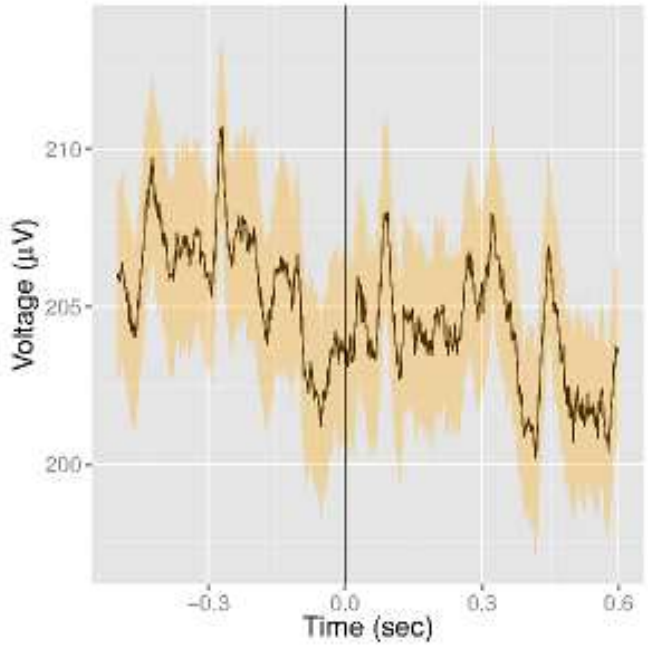

Figure A.34: ERP for electrode 132 computed from recordings in experimental session EC2_B105.

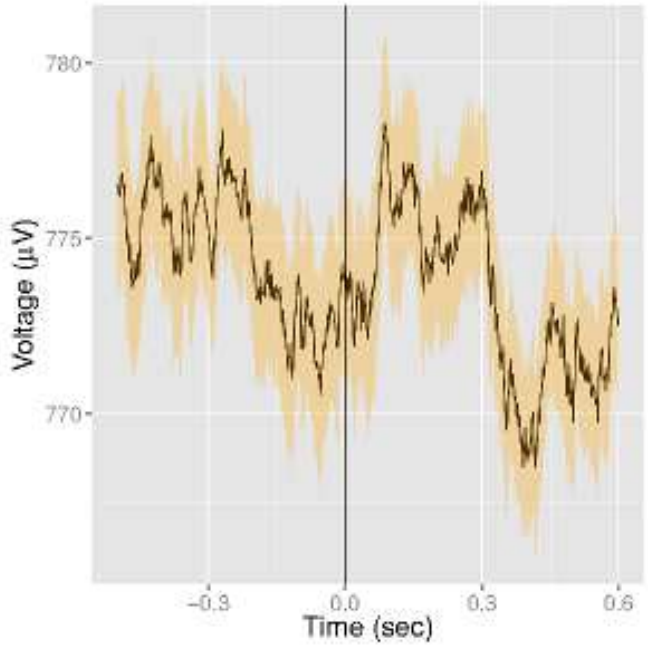

Figure A.35: ERP for electrode 133 computed from recordings in experimental session EC2_B105.

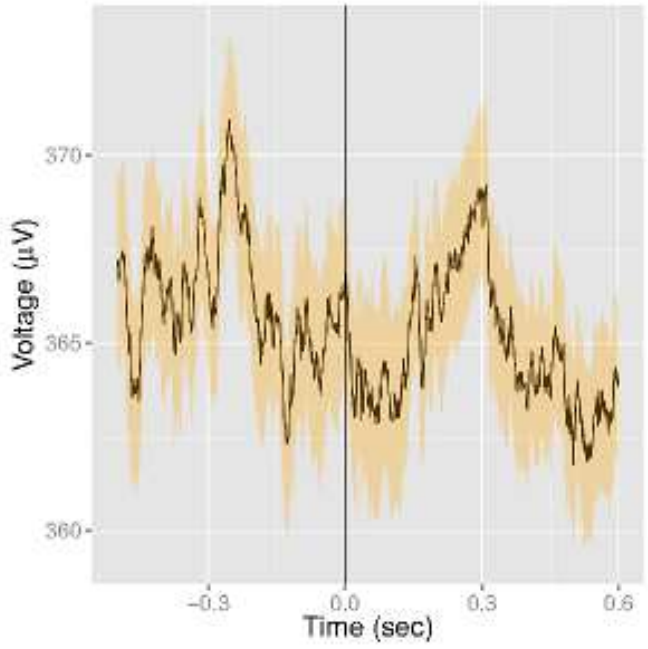

Figure A.36: ERP for electrode 134 computed from recordings in experimental session EC2_B105.

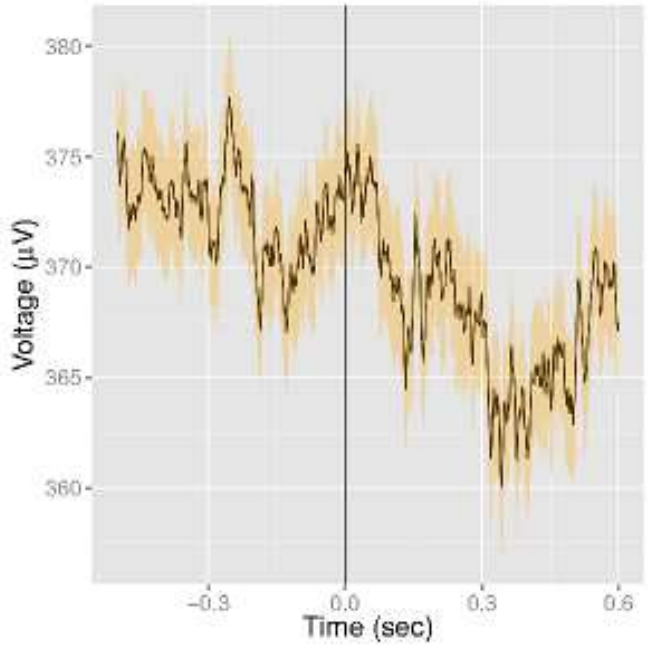

Figure A.37: ERP for electrode 135 computed from recordings in experimental session EC2_B105.

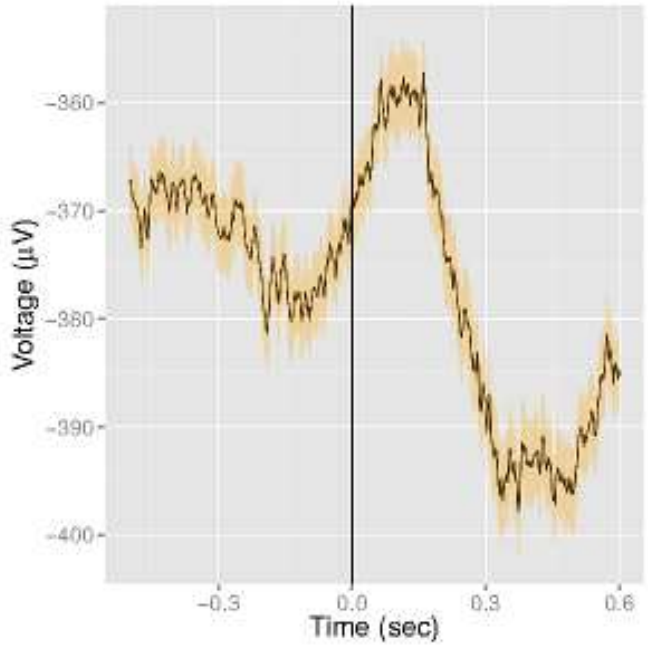

Figure A.38: ERP for electrode 136 computed from recordings in experimental session EC2_B105.

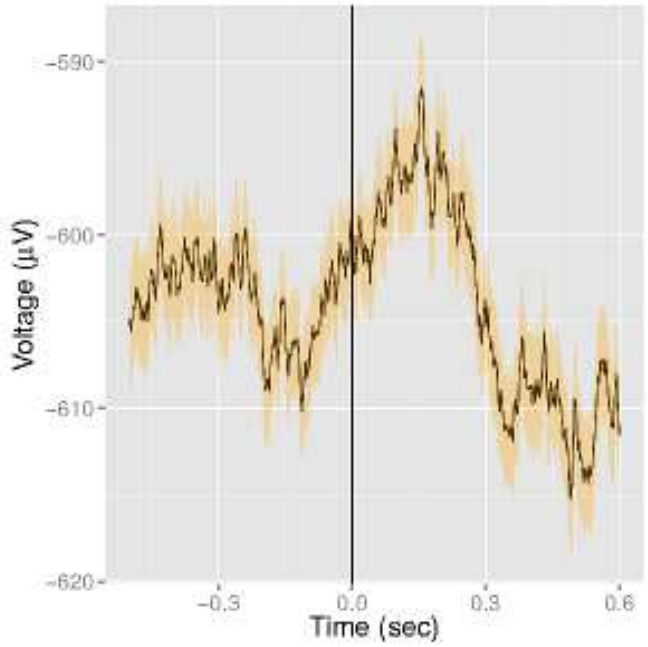

Figure A.39: ERP for electrode 137 computed from recordings in experimental session EC2_B105.

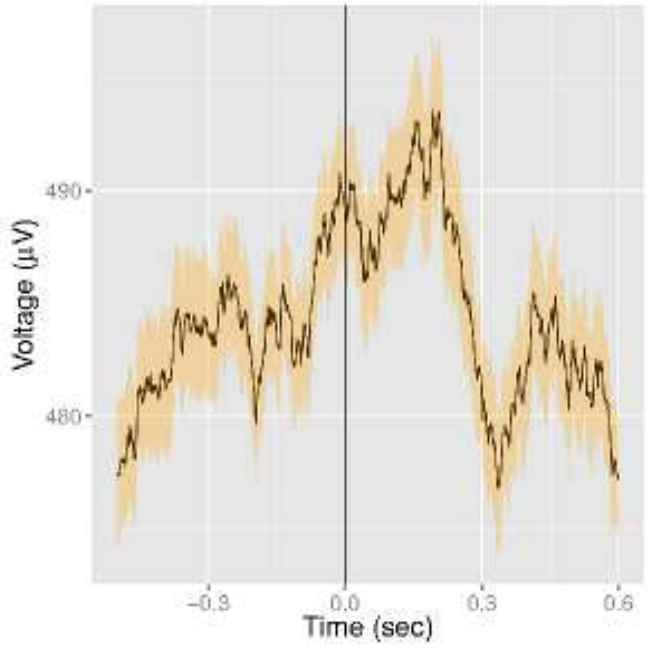

Figure A.40: ERP for electrode 138 computed from recordings in experimental session EC2_B105.

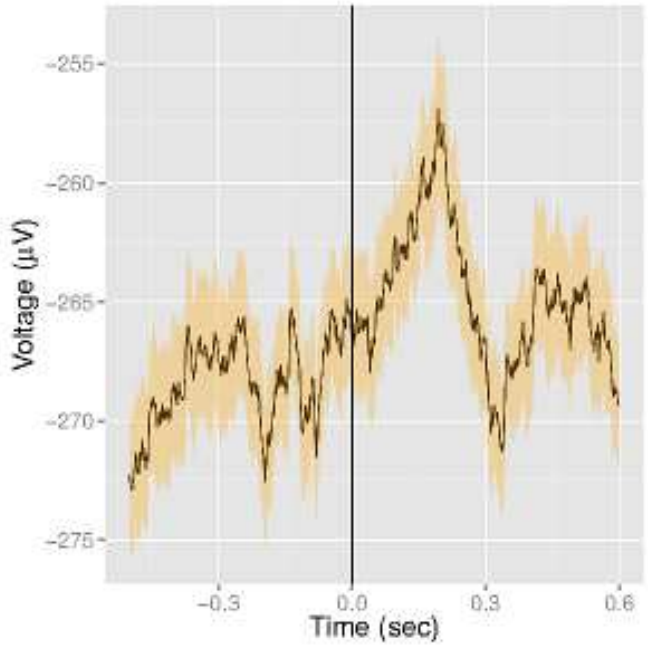

Figure A.41: ERP for electrode 139 computed from recordings in experimental session EC2_B105.

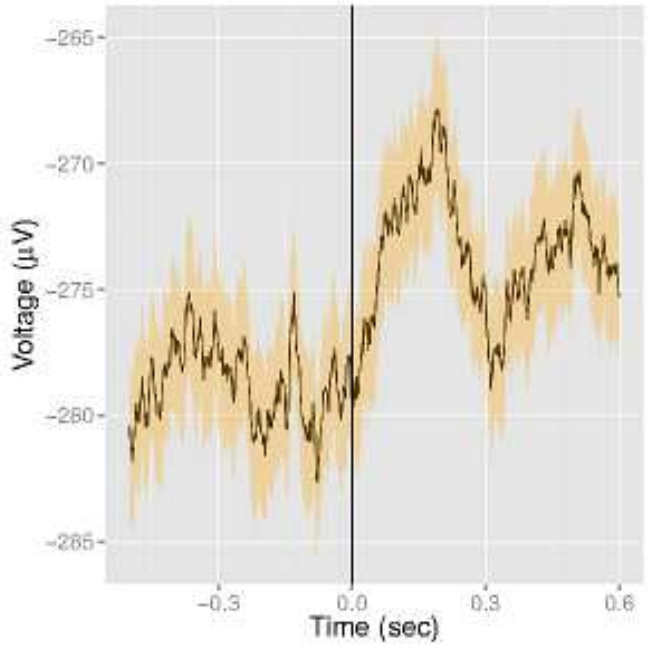

Figure A.42: ERP for electrode 140 computed from recordings in experimental session EC2_B105.

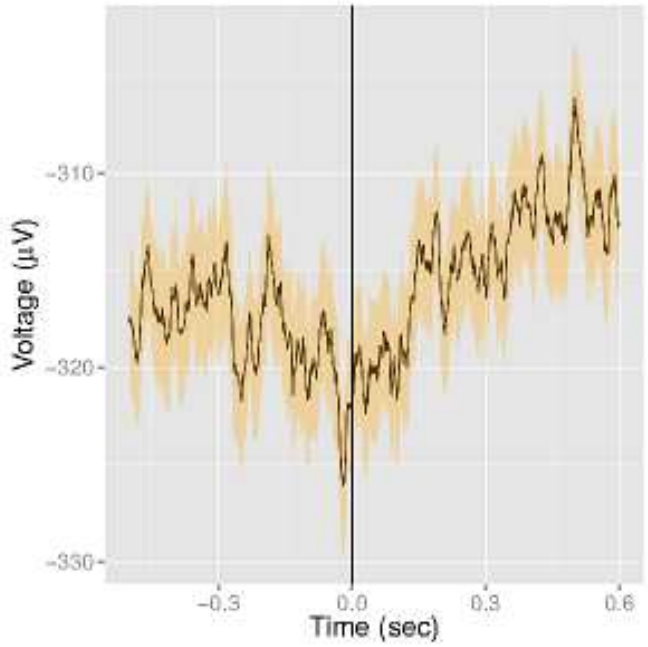

Figure A.43: ERP for electrode 141 computed from recordings in experimental session EC2_B105.

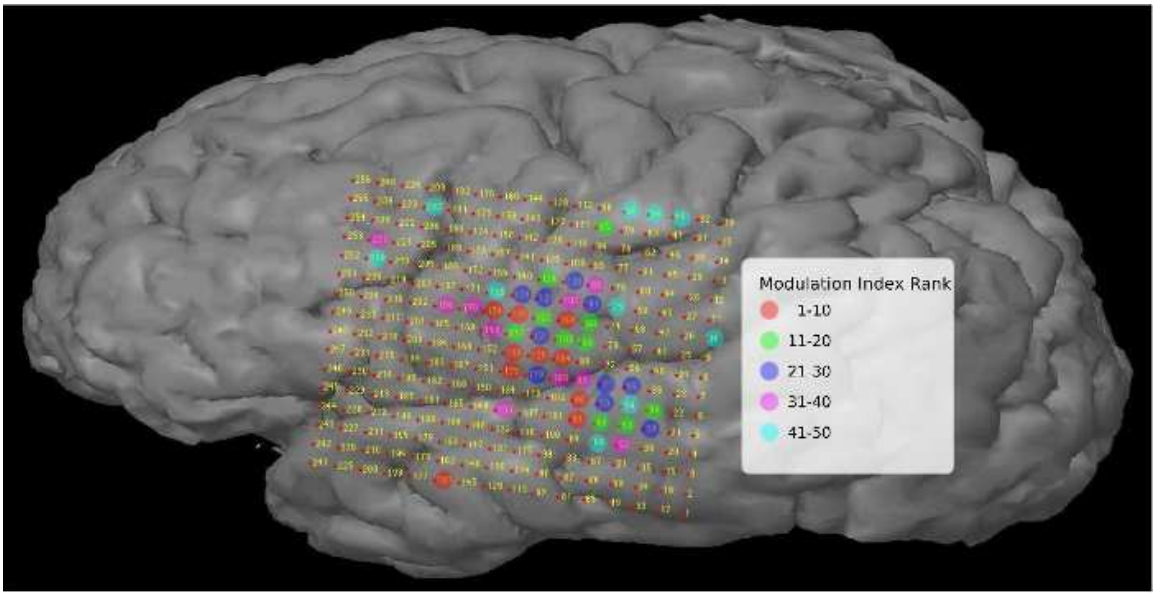

Figure A.44: Strongest PAC occurs over the vSMC. The 50 electrodes with largest MI (between 0.5 seconds before and 0.6 seconds after the CV transition, at the frequency of CV production, in the experimental session EC2_B105) are highlighted in color.